VERITAS Observations of the Blazar H 1426+428

By

Kayla Farrell, BSc

UCD Student Number: 15485328

This thesis is submitted to University College Dublin in fulfilment of the requirements for the degree of Research Masters

UCD School of Physics

Head of School: Professor Emma Sokell

Principal Supervisor: Associate Professor John Quinn

September 2022

Contents

Abstract

H 1426+428 is an extreme High frequency-peaked BL-Lac (HBL) blazar in the constellation Böotes. An HBL blazar is considered "extreme" when it has a synchrotron frequency $> 10^{17}$Hz. H 1426+428 is optically faint but very bright in the X-ray band. VERITAS is an array of four 12m Cherenkov imaging telescopes located at the Fred Lawrence Whipple Observatory (FLWO) near Tucson in Arizona. It is used for gamma ray astronomy in the $\sim$ 100 GeV – 30 TeV photon energy range. It uses the Imaging Atmospheric Cherenkov Telescope (IACT) technique, whereby gamma rays that cause particle showers in the earth's atmosphere are observed via the Cherenkov light produced. VERITAS observed H 1426+428 during an 8 year period of quiescence from 2008-2016 and during a period of higher activity in 2021. In this thesis both sets of VERITAS H 1426+428 data are analysed using VERITAS analysis software VEGAS. Very-high-energy (VHE) spectra are produced and corrected for extragalactic background light (EBL) absorption. Light curves are then produced on different timescales and investigated for flux variability. Multi-wavelength data was used from two upcoming VERITAS papers to compare the spectral energy distributions for both data sets to a synchrotron self-Compton (SSC) model. It was found that the SSC model could adequately explain both states.

Statement of Original Authorship

I hereby certify that the submitted work is my own work, was completed while registered as a candidate for the degree stated on the Title Page, and I have not obtained a degree elsewhere on the basis of the research presented in this submitted work.

This research was undertaken as a member of the VERITAS Collaboration. The VERITAS Collaboration provided the data, the analysis software and the instrument response functions (IRFs) needed to perform the analyses detailed in this thesis.

I provided the cross-check analysis on the data sets for two upcoming VERITAS publications on the blazar H 1426+428.

Collaborators provided the multi-wavelength data sets used in the modelling section of this thesis and are acknowledged appropriately. The modelling is my own work using publicly available software.

List of Figures

List of Tables

Chapter 1: Introduction

1.1 Blazars

Gamma-ray emission at energies in the MeV to > TeV range from objects in the cosmos are produced by non-thermal processes. Observations by instruments such as VERITAS enable us to study these relativistic processes, giving insight into the cosmic accelerators in which they occur.

Most, if not all galactic centres contain a supermassive black hole surrounded by an accretion disk of cold material [Kormendy and Ho, 2013]. Dissipative processes in the accretion disk transport matter inwards and angular momentum outwards. The matter falling inwards on the black hole produces gravitational energy, and this can power a relativistic outflow of material. Roughly 10% of active galaxies exhibit these outflows, correlating with strong emission in radio frequencies [Urry and Padovani, 1995]. These relativistic jets are highly collimated beams of radiation consisting of particles accelerated almost to the speed of light along the axis of rotation of the black hole (or the angular momentum axis of the accretion disk). These central nuclei tend to outshine the rest of the galaxy, and result in the galaxy having a much higher overall luminosity than is normal. This central core of highly variable and bright emission is called an Active Galactic Nucleus (AGN). An artist's interpretation of an AGN is shown in figure 1, and an image of an AGN taken by the Hubble Space Telescope is shown in figure 2.

AGNs are the most luminous persistent sources of electromagnetic radiation in the universe, producing the vast majority of light from galaxies. AGNs are generally split into three categories: quasars, blazars, and radio galaxies. In the past it was thought that these objects were three different kinds of galaxies, but astronomers now know that these are in fact the same object, but oriented at different viewing angles to Earth [Schilling, 2001]. A radio galaxy was thought to consist of two radio lobes at either side of the galaxy and little to no core activity. However, when viewed edge on the bright core of a quasar is hidden by a torus of dust, leaving only the two bright radio lobes visible. When one of the jets of the radio-emitting quasar is pointing directly towards earth, the object appears much more volatile and variable. When this is the case, we call it a blazar, and one of these objects is the focus of this research.

The radiation from a blazar is characterised by strong, diffuse, nonthermal radio emission, though blazars are visible in practically all bands, from the lowest observable frequencies (100 MHz, radio), to the highest (VHE gamma-rays in the multi-TeV

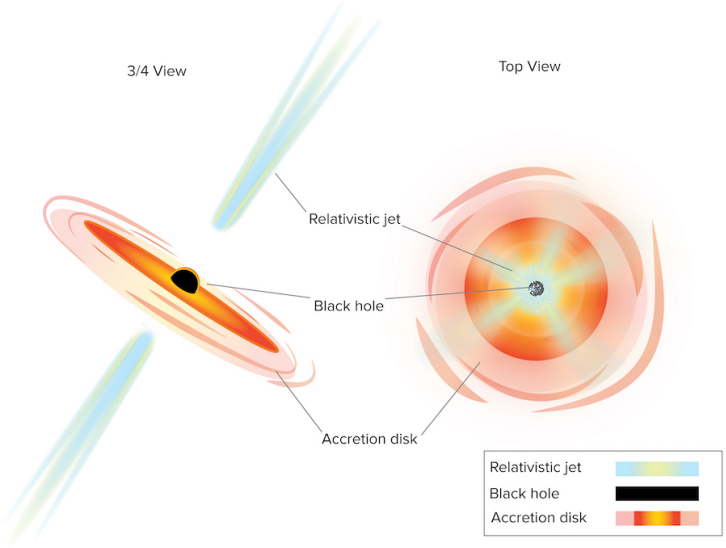

Figure 1: Artist's interpretation of an AGN (Credit: Sophia Dagnello, NRAO/AUI/NSF, astronomy.com)

range). These objects offer a unique opportunity to study particle species and energy distribution in a landscape beyond the standard model for particle physics. Blazars exhibit extreme variability (on the order of all timescales, from minutes to years). The shortest timescale indicates that the high-energy emission is produced near the centre of the galaxy, where the jet is produced and relativistic particles are accelerated. A small emission region is needed, to avoid the problem of gamma-ray photons pair producing with the low energy photons, resulting in the gamma-rays not escaping [Chen et al., 2015]. The ambient radiation in the background near the base of the jet can attenuate the gamma-ray signal also. For these reasons it is thought that the radiation must be beamed towards the observer, in order for us to detect it so brightly. The means by which these phenomena occur are not yet well understood, and so the gamma rays produced can give us a window into the inner-jet region [Vestrand, 2002].

Blazar spectra are an important source of information about these objects, and can shed light on emission mechanisms and possible emission models. Blazar broad-band spectra are smooth and without sharp features, and have a distinctive shape characterised by two humps (See figure 3). Blazars can be divided into two general subclasses, High frequency-peaked BL-Lac objects, and Flat Spectrum Radio Quasars (FSRQs). BL Lacs are named for the prototypical source, BL Lacertae, and have a higher synchrotron peak than FSRQs, but a lower intrinsic luminosity. These are

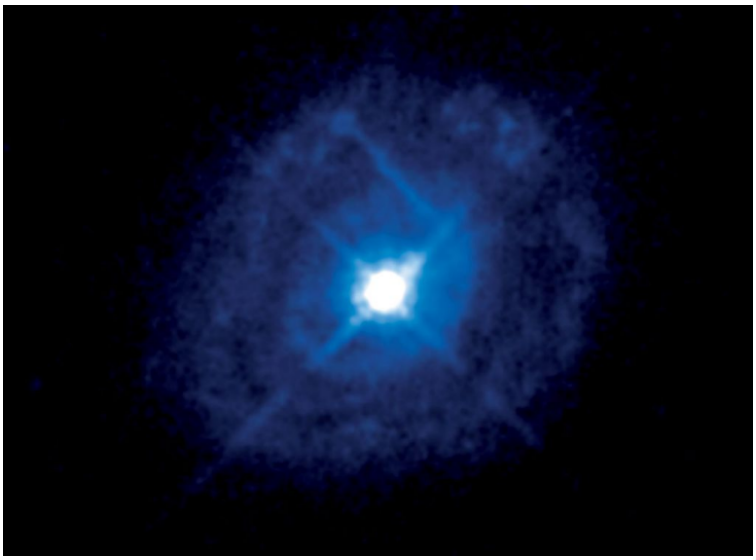

Figure 2: An image from the NASA/ESA Hubble Space Telescope of the galaxy Markarian 509. The bright object at the center of the galaxy is an active galactic nucleus. Credit: NASA, ESA, J. Kriss (STScI) and J. de Plaa (SRON)

Fanaroff-Riley Class I (FR-I) galaxies with most power concentrated towards the supermassive black hole at the base of the jet rather than the jet itself [Fossati et al., 1998]. (The Fanaroff-Riley classification is a system used to distinguish between radio galaxies and AGN based on their radio luminosity in relation to their background environment). Their accretion flow is radiatively inefficient and unable to ionize the surrounding gas [Fan and Wu, 2019].

BL Lacs can be divided into three categories based on the energy at which their synchrotron peak occurs: High Energy Peaked BL Lacs (HBLs), Intermediate Energy Peaked BL Lacs (IBLs), and Low Energy Peaked BL Lacs (LBLs), and each of these categories is theorised to require different emission mechanisms for the particles in the jet [Falomo et al., 2014]. BL Lacs are the most prominent source of gamma rays among the blazar population, and the majority of blazars detected at VHE (specifically HBLs precisely, these have the maximum synchrotron component). They show no emission lines in optical spectra [Landoni et al., 2014].

The emission from the accretion disk and surrounding dusty torus of a blazar is predominantly thermal and extends up to X-rays, while the relativistic particles in the jet produce broadband synchrotron and Compton emission, including gamma rays. For LBLs and IBLs, the synchrontron peak lies in infrared/optical to ultraviolet (UV). HBLs peak at soft to medium X-rays [Fossati et al., 1998].

FSRQs tend to be very bright, and can be classified as Fanaroff-Riley type 2 (FR-II) galaxies, where the power in the jet is concentrated in the outer lobes. They show prominent emission lines in optical spectra, produced by the clouds of gas orbiting around the central supermassive black hole and photoionized by UV photons from the disk [Ghisellini et al., 2009]. FSRQ intrinsic spectra are generally softer than BL Lacs. The best candidates for studying blazar spectra that deviate from standard models are BL Lacs, due to the high-energy photons we can detect from this subclass of blazars.

1.1.1 Spectral Energy Distributions (SEDs) and emission mechanisms

The spectral shape and strong polarization measured in blazars from the radio to optical bands suggest synchrotron origin, where the relativistic electrons or positrons radiate via change of their trajectories in a magnetic field [Madejski and Sikora, 2016]. This lower-energy emission characterises the first hump (radio to UV) of the blazar SED. There are two approaches taken to explain the second higher frequency hump (X-ray to gamma-ray): leptonic models or hadronic models.

In leptonic models an inverse-Compton mechanism is theorised to explain the gamma-ray emission. There are two scenarios: a synchrotron self-Compton (SSC) mechanism where the low-energy seed photons are the synchrotron photons [Kellermann and Pauliny-Toth, 1969], and an external radiation Compton (ERC) mechanism where the seed photons originate from areas external to the jet (such as from the Cosmic Microwave Background, stellar radiation, or diffuse infra-red radiation from the surrounding dusty torus). The synchrotron-self-Compton model fits well for HBL blazars, but LBLs often require different models, including ERC models. In hadronic models photon synchrotron models or photomeson production are thought to be the source of the radiation characterising the second spectral hump [Mastichiadis and Petropoulou, 2021].

Extreme HBL blazars also sometimes don't quite fit within the conventional one-zone SSC model. One alternative explanation that has been suggested to explain the observed TeV spectra is that protons from the blazar interact with background photons, producing secondary gamma rays along the line of sight [Essey and Kusenko, 2010].

A challenge that comes from studying objects at these energies and distances is the interaction of high energy photons with the optical UV radiation of the Extragalactic Background Light (EBL), resulting in severe absorption. How do these photons reach Earth so that we can detect them?

One possible scenario that could explain this would involve photons travelling and producing an electromagnetic cascade (in the absence of strong extragalactic magnetic fields), resulting in a hardened spectrum. Another scenario is that axion-like particles could be involved. A third possibility could be an enhancement of photon flux above 20 TeV, due to Lorentz invariant violation [Galanti et al., 2020].

The mechanism behind the production of the blazar jet has not yet been identifed, but the two most likely candidates are the rotational energy of the spinning black hole (where a jet-like outflow would be produced by the "frame dragging" of magnetic fields), or the gravitational energy of the accreting matter (the angular momentum of the disk magnetically being removed to launch the jet). There are also uncertainties regarding the content of the matter inside the jet (electron-proton or electron-positron plasma). There is a clear linear relationship between the accretion disk luminosity and the gamma ray power of the jets [Ghisellini et al., 2014], but the jet luminosity outshines that of the disk by more than an order of magnitude. This implies that the black hole's spin must also be involved along with the accretion disk. There is also a possibility that power is extracted from the disk by the magnetic field, causing it to appear fainter. Our understanding of the jet production mechanism is currently limited by our ability to measure the black hole spin.

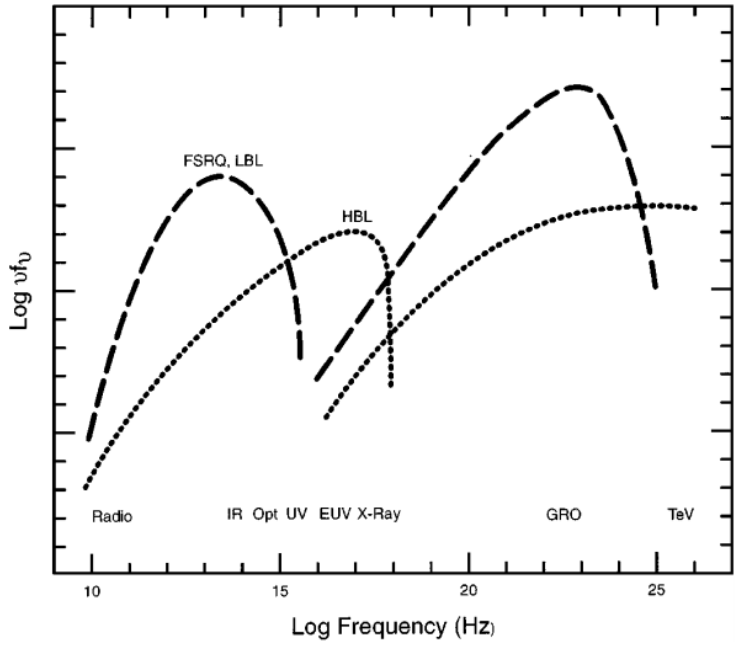

Figure 3: Broadband spectra of blazars [Ulrich et al., 1997]

1.2 Blazars observations at gamma-ray energies

Gamma-ray observations in the MeV-GeV range need to be carried out from space. The first satellites to detect celestial gamma-rays were the Orbiting Solar Observatory (OSO)-III in 1967, COS-B and then the Small Astronomy Satellite 2 (SAS-2) [Hartman et al., 1999]. The launch of the Energetic Gamma-ray Experiment Telescope (EGRET) as part of the Compton Gamma Ray Observatory (CGRO) greatly impacted studies of AGNs, discovering almost 200 gamma-ray sources, the majority being blazars [Casandjian and Grenier, 2008].

The Large Area Telescope (LAT) on board the Fermi Gamma Ray Space Telescope observes gamma-rays in the 20 MeV to greater than 300 GeV band. The majority of the sources detected by Fermi LAT (57%) are blazars. The Third LAT AGN Catalog contains 1563 gamma-ray sources associated with AGN, and of these 1563 sources, 1444 are associated with AGN with a very high confidence. This is the largest catalog of gamma-ray detected AGNs ever made [Ackermann et al., 2015].

Gamma-rays from astrophysical sources can be studied from the ground, at $>$ GeV energies due to the much larger effective collection area available. Imaging Atmospheric Cherenkov telescopes are ground based and use the Earth's atmosphere as a key part of the detection technique. They measure the Cherenkov radiation produced by energetic particles when gamma-rays interact with the atmosphere. Telescopes such as the Whipple 10-m Telescope, HEGRA (High-Energy-Gamma-Ray Astronomy), and CANGAROO (Collaboration of Australia and Nippon for a Gamma Ray Observatory in the Outback) pioneered this technique. Current Cherenkov VHE observatories such as VERITAS (Very Energetic Radiation Imaging Telescope Array System) [Park, 2015], MAGIC (Major Atmospheric Gamma-ray Imaging Cherenkov) [Aleksić et al., 2016], and HESS (High Energy Stereoscopic System)-II [Giebels and Collaboration, 2013] have extended the bandpass where blazars can be studied to much higher energies, and have found nearly 100 VHE emitting blazars. Data taken by VERITAS will be used in this thesis.

Blazars at energies above 20 - 30 TeV can help shed light on the current incomplete models for emission, as it is at these energies that measured spectra start to deviate from standard spectra produced by leptonic and hadronic models.

In recent years, multiwavelength observations (multiple telescopes observing the same source simultaneously at different wavelengths) of blazars have been useful in unveiling the mechanisms behind the production of radiation. Spectra at each wavelength must be observed simultaneously, because blazars vary at all wavelengths.

1.3 H 1426+428

H 1426+428 is an extreme HBL in the constellation Böotes with a synchrotron peak located at $10^{18.1}$Hz [Costamante et al., 2001]. An HBL blazar is considered "extreme" when it has a synchrotron frequency $> 10^{17}$Hz. H 1426+428 is an optically faint object but is bright in the X-ray band. It is thought to be at the centre of an elliptical galaxy.

H 1426+428 was first detected in X-ray in the 1970's by the Uhuru X-ray observatory [Giacconi et al., 1972], and was classified as a Bl Lac by Remillard et al. [1989] during an observational program to find optical and radio counterparts of X-ray sources from the HEAO 1 survey. In 1985, optical spectra were taken by Remillard et al. [1989], revealing a set of weak absorption features and a redshift of z=0.129.

H 1426+428 was first detected at gamma-ray energies by the Whipple imaging atmospheric Cherenkov Telescope (IACT) [Horan et al., 2002], and its first detection by a gamma-ray satellite was in 2009 by the Fermi Large Area Telescope (LAT) [Abdo et al., 2009] (it was not detected by EGRET). It was subsequently detected by CAT [Aharonian et al., 2002] and HEGRA [Djannati-Atai et al., 2002]. Its VHE (E > 100 GeV) flux ranged up to 80% of the Crab Nebula (Crab Units, C.U.) above a few hundred GeV, and was seen to be very variable.

In this thesis, VERITAS observations of H 1426+428 will be analysed, and the spectrum of this source will be compared with a synchrotron self compton model.

Chapter 2: Blazar physics

Blazar broadband spectral energy distributions (SEDs) generally follow a double-humped shape. These humps characterise two general subclasses, Bl-Lac objects, and Flat Spectrum Radio Quasars (FSRQs).

For the low-frequency emission which appears as the first hump on the blazar SED (radio to UV), it is generally accepted that the source is inverse-Compton emission from the jet. For the second higher-frequency hump (X-ray to gamma-ray), two approaches can be taken; a leptonic model or a hadronic model. While leptonic models attribute this radiation to a synchrotron self-compton mechanism (see below), hadronic models explain the emission using proton synchroton models or photomeson production. In leptonic models, the radiative output is dominated by electrons or sometimes positrons, while protons are not accelerated to sufficiently high energies to contribute to the overall flux [Böttcher et al., 2013]. The majority of blazar models are leptonic, as hadronic models can be much more complicated to implement

due to a sequence of particle decay, involving $p\gamma$ photo-pion production [Mannheim and Biermann, 1992]. Multi-zone models have also been proposed [Tavecchio and Ghisellini, 2008].

In chapter 5 of this thesis we will attempt to match an SSC model to the SED of the HBL blazar H1426+428.

2.1 Doppler boosting and jets

Blazar emission is dominated by the presence of a relativistic jet of plasma that moves at almost the speed of light. A schematic of a blazar jet is shown in figure 4. The matter in the jet is accelerated and collimated by strong, helical magnetic fields, and standing and moving shocks can be produced by the plasma inside the jet. Particle acceleration can happen in these areas, and this will dominate emission in parts of the blazar SED.

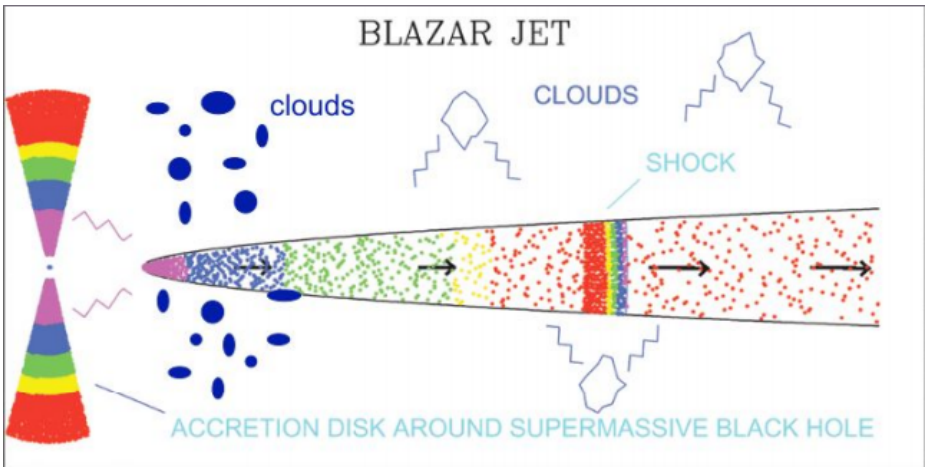

Figure 4: Schematic of a blazar jet [Barat et al., 2022]

Relativistic beaming (or Doppler boosting) plays a large part in why we are able to observe high-energy radiation from such distant sources. This is the process by which the apparent luminosity of emitting matter moving at speeds close to the speed of light, c, along the line of sight is modified by relativistic effects - the light will appear to be brighter. The opposite can also occur when the radiation is oriented away from the line of sight - the light will appear dimmer. Boosting (and de-boosting) occurs when a compact object like a blazar has two oppositely directed relativistic jets of plasma.

The observed luminosity will depend on the speed of the jet, the properties of the particles inside the jet (such as spectral index), and the angle to the line of sight. If the jet is oriented with angle θ_{obs} with respect to our line of sight, this results in Doppler boosting characterised by relativistic Doppler factor: [Böttcher et al., 2013]

$$\delta = \frac{1}{\Gamma(1 - \beta \cos \theta_{obs})}$$

where $\gamma = (1 - \beta^2)^{-\frac{1}{2}}$ is the Lorentz factor, $\beta = \frac{v}{c}$ is the plasma velocity in units of the speed of light, and θ_{obs} is the angle between the velocity vector and the line of sight in the rest frame. This factor determines the Lorentz boost of the observed frequency.

Time dilation implies: $t_{obs} = \frac{t_s}{\delta}$; $v_{obs} = \delta v_s$; $E_{obs} = hv_{obs} = \delta h v_s = \delta E_s$ [Rybicki and Lightman, 1991]

Due to the doppler boosting, the observed variability timescale is reduced, and the observed frequencies and the observed flux are increased. $I(v)/v^3$ is Lorentz invariant ($I(v)$ being the specific intensity at frequency v) [Lightman and Rybicki, 1979]. Therefore:

$$\frac{I_{obs}(v_{obs})}{v_{obs}^3} = \frac{I_s(v_s)}{v_s^3}$$

$$I_{obs}(v_{obs}) = I_s(v_s)\frac{v_{obs}^3}{v_s^3} = I_s(v_s)\delta^3$$

The observed specific intensity is boosted by a factor of δ^3. So for the total intensity integrated over all energies:

$$I_{obs} = \int_0^\infty I_{obs}(v_{obs}) dv_{obs} = \int_0^\infty \delta^3 I_s(v_s) \delta dv_s = \delta^4 I_s$$

The doppler factor has a strong dependence on the viewing angle - the larger the Lorentz factor, the stronger the dependence. The Doppler factor is unity for $\theta_D = \arccos(\sqrt{(\Gamma - 1)/(\Gamma + 1)})$, and for angles larger than θ_D relativistic deamplification (de-boosting) will take place.

The observed luminosity can be related to the intrinsic luminosity in a simple jet model of a single homogeneous sphere using the beaming equation:

$$S_o = S_e \delta^p$$

with $p = 3 - \alpha$ (alpha is spectral index), and δ= Doppler factor.

The observed luminosity will therefore depend on the speed of the jet, the properties inside the jet (such as spectral index), and the angle to the line of sight through the Doppler factor. The beaming equation effectively encapsulates three effects: relativistic aberration, time dilation, and blue or redshifting.

The relative Doppler shift for an electron at rest in a moving frame with speed parameter β is given by:

$$h\nu' = \left(\frac{1+\beta}{1-\beta}\right)^{\frac{1}{2}} h\nu$$

Doppler boosting can help explain why quasars and blazars weren't always considered the same object. The jet from a quasar facing Earth is boosted (Doppler factor = 2Γ, see below), and the jet facing away is de-boosted, giving the illusion that there is just one very bright jet. This is why blazars, which face earth head-on, dominate at gamma-ray energies. Radio galaxies exhibit both a jet and a counterjet, because they are viewed side-on.

So in the highly relativistic case ($\beta \approx 1$):

$$\left(\frac{1+\beta}{1-\beta}\right)^{\frac{1}{2}} \xrightarrow[\beta \approx 1]{} 2\Gamma$$

2.2 Synchrotron radiation

Synchrotron emission (or magnetobremsstrahlung) is produced when relativistic charged particles are accelerated due to the presence of a magnetic field (see figure 5). The stronger the magnetic field and the higher the energy of the particles, the greater the intensity and the frequency of the emitted radiation. Synchrotron radiation is highly polarised, vertically collimated and has a non-thermal power law spectrum. When the particle is non-relativistic, the emission is called cyclotron emission.

The spectral power (power radiated at frequency ν) [Rybicki and Lightman, 1991] by an electron of energy $\gamma m_e c^2$, moving at a speed of $\beta = \frac{\nu}{c}$ in a magnetic field B at a pitch angle (the angle between the magnetic field and the particle velocity) α is given by:

$$P(\nu, \gamma) = \frac{\sqrt{3} e^3 B \sin(\alpha)}{m_e c^2} F\left(\frac{\nu}{\nu_c}\right)$$

with

$$\nu_c = 1.5\gamma^2 \nu_L \sin(\alpha)$$

where $\nu_L = \frac{eB}{2\pi m_e c}$ is the Larmor frequency, and ν_c is the critical frequency. The synchrotron power function $F(x)$ [Rybicki and Lightman, 1991] is given by:

$$F(x) = x \int_x^\infty K_{\frac{5}{3}}(z) dz$$

where $K_{\frac{5}{3}}$ is the modified Bessel function.

The shape of the spectrum will be governed by $F(\frac{\nu}{\nu_c})$, and this peaks at $\sim 0.29(\frac{\mu}{\mu_c})$ (see figure 6). We can find the total radiated power by an electron with pitch angle α using the equations above:

$$P(\gamma, \alpha) = 2c\sigma_T \beta^2 \gamma^2 \frac{B^2}{8\pi} \sin^2 \alpha$$

where σ_T is the Thomson scattering cross-section. The average power radiated per particle can be obtained by averaging over the velocity field:

$$P_{syn}(\gamma) = \frac{1}{4\pi} \int P(\gamma, \alpha) \sin \alpha \, d\Omega$$

$$= \frac{1}{8\pi} c\sigma_T \beta^2 \gamma^2 B^2$$

for an isotropic power-law electron distribution described by:

$$N(\gamma) = K\gamma^{-\zeta}$$

It can be shown that the resulting synchrotron spectrum will be a power-law distribution with spectral index $-\frac{(\zeta-1)}{2}$ [Fouka and Ouichaoui, 2014]. A power law superposition of the synchrotron radiation spectrum for one electron and a group of electrons can be seen in figure 6.

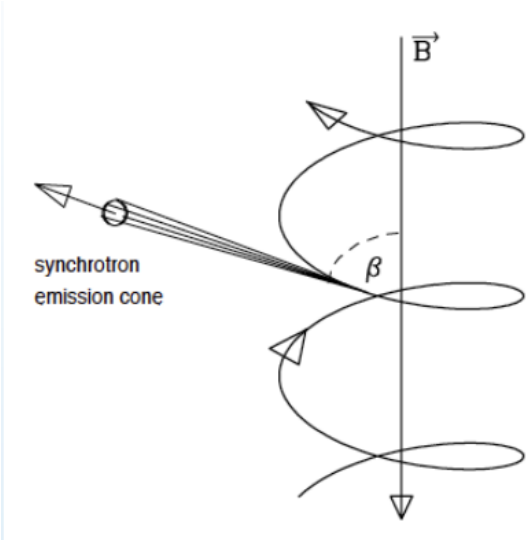

Figure 5: Synchrotron emission (Beckmann and Shrader (2012))

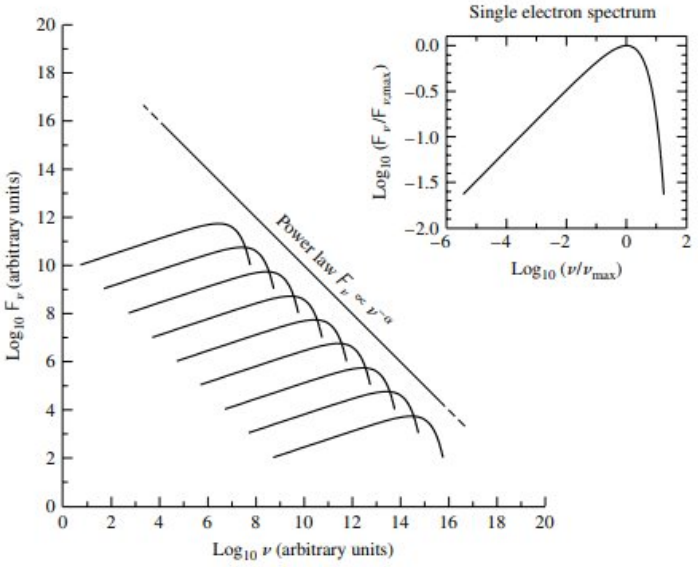

Figure 6: Power law superposition of the synchrotron radiation spectrum for one electron (top right) and a group of electrons (left) [Carroll and Ostlie, 2017]

2.3 Compton and inverse-Compton Scattering

2.3.1 Compton scattering

Compton scattering occurs when a photon interacts with a stationary free electron, and the electron gains the energy the photon loses as it is scattered into angle θ. The photon energy relative to the electron energy determines the scattering cross-section. If the energy of the incoming photon and the scattered photon energy is much less than that of the electron energy, we can ignore the electron recoil and treat the scattering as if in the Thomson regime.

The initial energy of the electron is assumed to be zero, with recoil energy γmc^2 and momentum $p = \gamma\beta mc = \gamma m\nu$ (where ν is recoil speed, m is rest mass, $\beta = \frac{\nu}{c}$, $\gamma = (1-\beta^2)^{-\frac{1}{2}}$, and the energy and momentum of the incoming and scattered photon are $h\nu$ and $\frac{h\nu}{c}$, and $h\nu_s$ and $\frac{h\nu_s}{c}$, respectively).

The equations of energy conservation, longitudinal momentum, and transverse momentum will be used to derive the Compton wavelength shift:

$$h\nu + mc^2 = h\nu_s + \gamma mc^2$$
$$\frac{h\nu}{c} = \frac{h\nu_s}{c}\cos\theta + \gamma\beta mc\cos\phi$$
$$0 = \frac{h\nu_s}{c}\sin\theta - \lambda\beta mc\sin\theta$$

Where ϕ is the angle of the scattered photon and θ is the angle of the scattered electron with respect to the direction of the incident photon (see figure 7) [Venugopal and Bhagdikar, 2012]. The left-hand-side of these equations represent the initial (prior to the interaction) momentum and energy.

Solving the longitudinal momentum equation for $\cos\phi$, the tranverse momentum equation for $\sin\phi$, and substituting in the identity:

$$\cos^2\phi + \sin^2\phi = 1$$

To get:

$$h^2(\nu^2 + \nu_s^2 - 2\nu\nu_s\cos\theta) = (\gamma\beta mc^2)^2$$

Squaring the energy conservation equation and rearranging:

$$h^2(\nu^2 - 2\nu\nu_s) + 2hmc^2(\nu - \nu_s) + m^2c^4 = (\gamma mc^2)^2$$

And subtracting the first from the second:

$$-2h^2\nu\nu_s(1-cos\theta)+2hmc_\nu^2-\nu_s+m^2c^4\gamma^2(1-\beta^2)$$

$$\gamma^2(1-\beta^2)=1, \text{ from the definition of } \gamma$$

therefore:

$$\frac{1-\cos\theta}{mc^2}=\frac{\nu-\nu_s}{h\nu\nu_s}$$

$$\frac{1}{h\nu_s}-\frac{1}{h\nu}=\frac{1-\cos\theta}{mc^2}$$

using $\nu=\frac{c}{\lambda}$:

$$\lambda_s-\lambda=\frac{h}{mc}(1-\cos\theta)$$

This can be rearranged to obtain the convenient form of the Compton relation between the incoming and scattered wavelengths:

$$h\nu_s=\frac{h\nu}{1+\frac{h\nu}{mc^2}(1-\cos\theta)}$$

There will be no significant reduction in energy when the photon is scattered at low energies, and decrease in energy will be greatest when the photon is back-scattered. As the photon energy $h\nu$ becomes comparable to the rest energy of the electron (mc^2), the scattered energy is shifted significantly. For very high photon energies ($h\nu \gg mc^2$), the energy of the back-scattered photon will be $\frac{mc^2}{2}$ irrespective of the incoming photon energy.

2.3.2 Inverse-Compton scattering

When the electron interacts with a high energy electron, resulting in the photon gaining some of the electron's energy (see figure 8), this is called Inverse-Compton scattering. Photons can be scattered up to gamma-ray energy ranges due to the high energy gain.

The electron is initially at rest in the Compton scattering scenario. For the Inverse-Compton scenario we can simply transform to the frame of reference where the electron is at rest, and then apply the Compton scattering formula. To get the increase in photon energy after the interaction we then transform back to the observer frame.

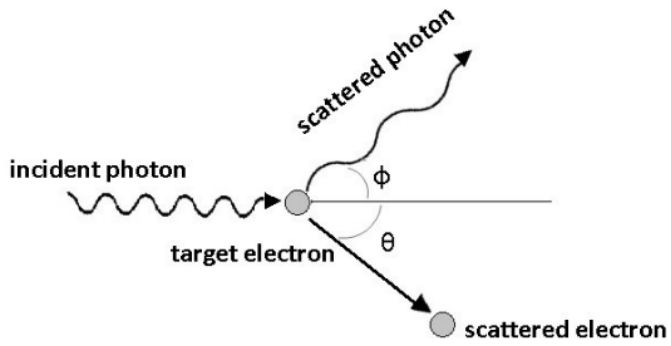

Figure 7: Compton scattering [Venugopal and Bhagdikar, 2012]

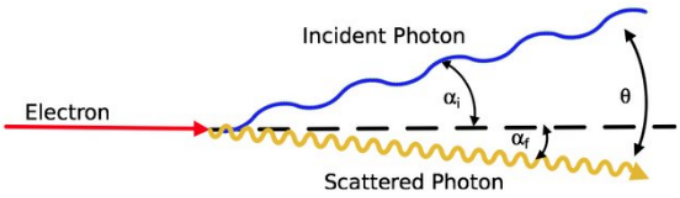

Figure 8: Inverse Compton scattering [Ertley, 2014]

Below we discuss the simplest scenario, where the photon is back-scattered in the electron's frame of reference (therefore attaining the maximum possible energy):

The electron is at rest in the moving frame S', which has speed parameter β. The relative Doppler shift gives:

$$h\nu' = \left(\frac{1+\beta}{1-\beta}\right)^{\frac{1}{2}} h\nu$$

Because the electron is initially at rest in S', the Compton scatter (in S') obeys the Compton formula. When the photon is back-scattered:

$$h\nu'_s = \frac{h\nu'}{1 + \frac{2h\nu^{2\prime}}{mc^2}}$$

The photon loses energy, and this is given to the electron. If $2h\nu' \ll mc^2$, the energy shift is small.

The velocity of the scattered photon in S' is in the same direction as S, so the reverse transformation back to the S frame will result in a second Doppler shift:

$$h\nu_s = \left(\frac{1+\beta}{1-\beta}\right)^{\frac{1}{2}} h\nu_s$$

Now $h\nu_s$ in S needs to be expressed in terms of the original photon energy $h\nu$ in frame S. We assume that the initial electrons are highly relativistic ($\beta \approx 1$) and so can use:

$$\left(\frac{1+\beta}{1-\beta}\right)^{\frac{1}{2}} \xrightarrow[\beta \approx 1]{} 2\gamma$$

Substituting the formula for the first Doppler shift into the formula for the Compton scatter in S':

$$h\nu_s \approx 4\gamma^2 h\nu \left(1 + \frac{4\gamma h\nu}{mc^2}^{-1}\right)$$

where γ is the Lorentz factor of the high-energy electron that collides with the photon of energy $h\nu$, and mc^2 is the rest energy of the electron.

With the condition $4\gamma h\nu \ll mc^2$:

$$h\nu_s \approx 4\gamma^2 h\nu = 4\frac{U}{mc^2} h\nu$$

Where γ has been expressed as the ratio of the total (rest + kinetic) energy of the electron U to the rest energy mc^2. This boost of γ^2 is an important result. It means that an electron with a Lorentz factor of 10^3, for example, will result in a boost factor of 10^6, taking the energy range from X-ray to gamma-ray.

2.3.3 Klein-Nishina cross-section

The scattering cross-section depends on energy, and for small values of $\frac{hv}{m_e c^2}$ this will be the Thomson cross-section (scattered photon energies $\sim \gamma_e^2 hv$, where γ_e is the electron Lorentz factor and hv is the soft photon energy) [Kusunose and Takahara, 2005], given by:

$$\sigma_T = \frac{8\pi}{3} r_0^2$$

Where $r_0 = \frac{1}{4\pi\epsilon_0} \frac{e^2}{m_e c^2}$.

In the case where the photon's energy is greater than or comparable to the electron rest energy, the recoil of the electron becomes considerable and we must use the Klein-Nishina cross-section (scattered photon energies $\sim \gamma_e h\nu$). Quantum effects are included in this case.

The integral Klein-Nishina cross-section [Yazaki, 2017] in the rest frame of a free electron is given by:

$$\sigma = 2\pi r_e^2 \left\{ \frac{1+\epsilon}{\epsilon^2} \left[\frac{2(1+\epsilon)}{1+2\epsilon} - \frac{1}{\epsilon} ln(1+2\epsilon \right] + \frac{1}{2\epsilon} ln(1+2\epsilon) - \frac{1+3\epsilon}{(1+2\epsilon)^2} \right\}$$

where r_e is the classical electron radius and $\gamma = h\nu / m_e c^2$ is the scaled energy of the incident photon.

The electron loses almost all of its energy to the photon in a single scattering in the extreme Klein-Nishina regime, whereas in the Thomson regime it only loses a small fraction of it's energy in each scattering. This results in quite a steep spectrum in the extreme Klein-Nishina case. A Klein-Nishina total cross-section as a function of energy is shown is figure 9.

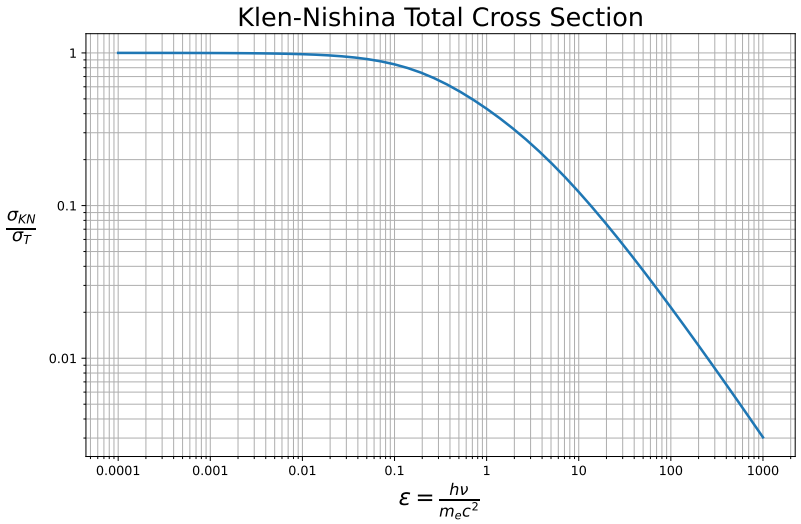

Figure 9: Klein-Nishina total cross-section

In leptonic models, the inverse-Compton process is thought to be responsible for the high-energy component of the blazar SED [Fields, 2007].

2.4 Synchrotron Self Compton and External Inverse-Compton models

Blazar spectral energy distributions (SEDs) are a measure of power observed at each frequency (νF_ν vs ν, or equivalently $E^2 dN dE$ vs ν). They follow a pattern where the peak energy of the synchrotron emission spectrum decreases with increasing luminosity [Fossati et al., 1998]. Blazar broadband spectra, when plotted, generally are lineless and show two distinct humps (see figure 3). Below and above the peaks, the spectrum is quite smooth and can be approximated with power-law profiles. The observed spectral shape requires that the relativistic electron spectrum steepens with increasing energy. This behaviour can be approximated with a broken power-law [Tavecchio et al., 1998].

For the low-frequency emission which appears as the first hump on the blazar SED (radio to UV), it is generally accepted that the source is synchrotron emission from the jet.

Two approaches can be taken to explain this second hump; leptonic models or hadronic models. In leptonic models, the second higher-frequency hump (X-ray to gamma ray) is thought to be the result of inverse-Compton scattering. There are several possible explanations for the source of the low energy photons involved in this inverse-Compton scattering, including synchrotron-self-Compton (SSC) scattering, and external inverse compton (EIC) scattering.

Sycnhrotron-self-Compton scattering occurs when the photons scattered to higher energies in the inverse-Compton process at the high-energy end of the blazar SED come from the same population of synchrotron photons that produce the first blazar peak [Maraschi et al., 1992].

In the simplest case, emission is assumed to come from a single emission zone of specified geometrical shape. Consider a homogeneous blob moving with bulk Lorentz factor Γ, which emits gamma-rays by the Inverse Compton process. The radius of the blob (as indicated by the variability timescale and corrected for relativistic beaming effects) is $R = ct_{var}\delta/(1+z)$, where δ is the Doppler factor. Describing the spectrum of the electrons in the double-humped SED using a broken power-law with spectral indices smaller and larger than 3 [Ghisellini et al., 1996], respectively below and above a break energy γ_b (in units of $m_e c^2$), the maximum in the power per decade emitted

via the synchrotron and inverse-Compton mechanisms is due to electrons of energy corresponding to γ_b. The observed frequency of the peak of the synchrotron SED is given by:

$$\nu_s \simeq (4/3)\nu_B \gamma_B^2 \delta/(1+z)$$

where $\nu_B = 28 \times 10^6$Hz is the Larmor frequency.

The maximum in the power per decade of the inverse-Compton emission occurs at an observed frequency of $\nu_c \simeq (4/3)\gamma_b^2 \nu_s$, therefore the energy of the electrons that contribute most to the power output can be derived if the frequency of the two peaks (ν_s and ν_c) are determined from observations [Ghisellini et al., 1996]:

$$\gamma_b \simeq \left(\frac{3\nu_c}{4\nu_s}\right)^{\frac{1}{2}}$$

This is the electron break energy.

In more complicated models multi-emission zones or jet structures are used, such as models with a jet composed of a fast spine in a slow layer [Ghisellini et al., 2005], a slow jet component in front of a fast base [Georganopoulos and Kazanas, 2003], or a small acceleration region inside a larger emitting region [Chen et al., 2015].

HBL SEDs are well described by SSC models. FSRQs, LBLs and IBLs tend to require external radiation fields. EIC models can be used to accurately describe the SEDs of these objects. In EIC models, a similar emission region to SSC is used, but an additional photon field from the accretion disk, the broad-line region, or the dusty torus is included. Photons from these regions can then be up-scattered on the electron population. The different kinds of blazars and their corresponding synchrotron peaks and inverse-Compton peaks are illustrated in figure 10.

While leptonic models attribute this radiation to a synchrotron self-Compton mechanism, hadronic models explain the emission using photon synchrotron models or photomeson production. In leptonic models, the radiative output is dominated by electrons or sometimes positrons, while protons are not accelerated to sufficiently high energies to contribute to the overall flux. The majority of blazar models are leptonic, as hadronic models can be much more complicated to implement due to a sequence of particle decay, involving $p\gamma$ photo-pion production [Mannheim and Biermann, 1992]. Multi-zone models have also been proposed [Tavecchio and Ghisellini, 2008].

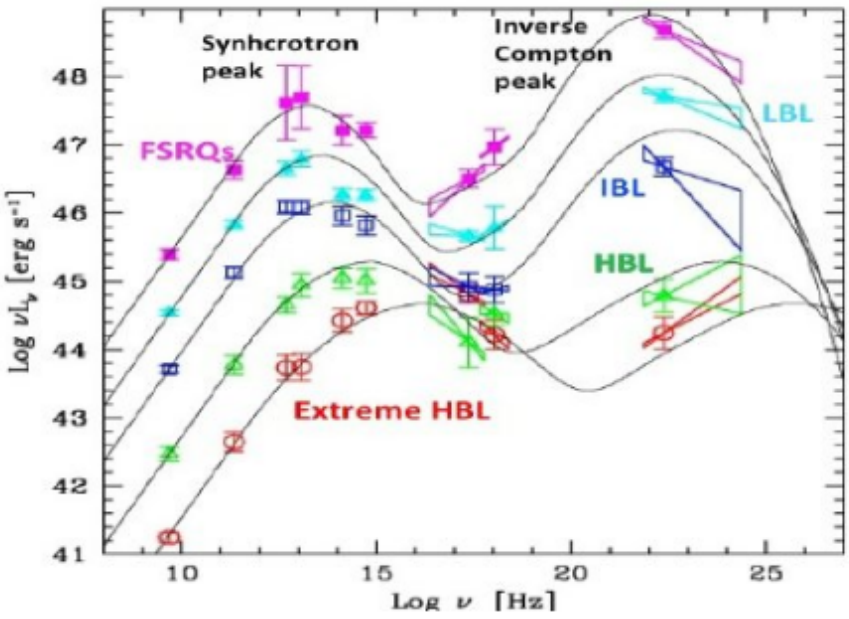

Figure 10: Blazar SED sequence

2.5 Extragalactic Background Light

The Extragalactic Background Light (EBL) is the integrated intensity of all the light emitted throughout the history of the universe. It extends from the far-infrared through visible and into ultraviolet. It is thought to be dominated by starlight, either through direct emission or through absorption and radiation by dust. The SED of the EBL is shown in figure 11. High-energy gamma rays will be absorbed by the EBL via pair-production. This creates difficulties when attempting to observe very far away blazars. Due to contamination by foreground zodiacal and galactic light, it is difficult to measure the EBL for TeV photons.

A gamma-ray photon with energy E penetrating through an isotropic field of photons can interact with any background photon of energy $\epsilon = (m_e c^2)^2/E \approx 0.26(\text{E}/1\ \text{TeV})^{-1}\text{eV}$ [Guy et al., 2000].

The observed spectra F_{obs} are modified by gamma-gamma pair production:

$$F_{obs}(E) = F_{int}(E) \exp\left[-\tau_{\gamma\gamma}(E, z)\right]$$

where $\tau_{\gamma\gamma}$ is the optical depth. This effectively creates a "gamma-ray horizon" that limits observations depending on the threshold of the telescope used.

We can use an EBL absorption model (such as Francescini et al (2008), Finke et al (2010), Dominguez et al (2011)) to attempt to replicate the true gamma ray spectrum by removing the effects of the EBL, or to add absorption to theoretical models to compare the model with observational data (as is done in chapter 5 of this thesis using Francescini et al (2008)). The surviving flux fraction for H 1426+428 after EBL absorption is shown in figure 12.

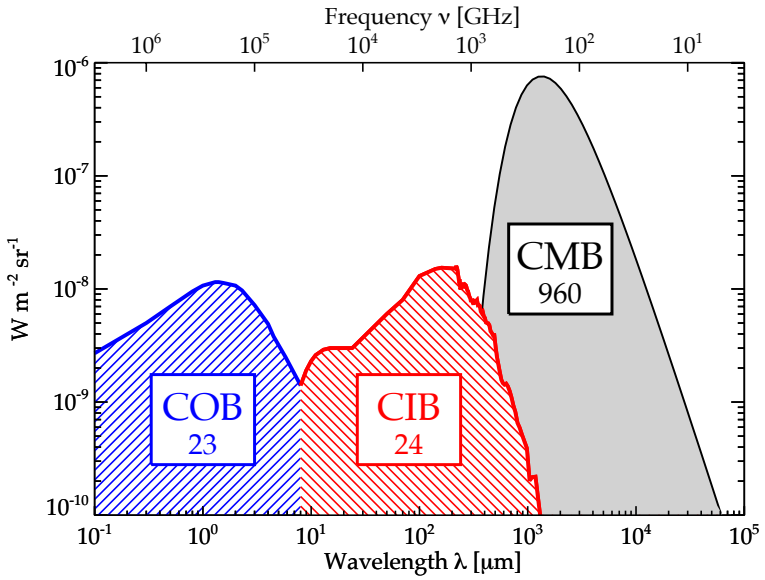

Figure 11: SED of the EBL [Dole et al., 2006], including cosmic optical background (COB), cosmic infrared background (CIB) and cosmic microwave background (CMB).

2.6 AGNPy

AGNpy is an open-source python package for modelling the radiative processes of relativistic particles accelerated in the jets of AGN [Nigro et al., 2021]. The classes included describe the galactic components responsible for line and thermal emission (from the cosmic microwave background (CMB), the accretion disk, the broad line region, and the dust torus), calculate the absorption due to $\gamma\gamma$ pair production on several photon fields, and provide the absorption due to the EBL. Deriving non-thermal energy distributions for this emission is important for our understanding of the jet composition and the acceleration mechanism. AGNpy parameterises the acceleration, escape, and radiation processes to assign maximum and break Lorentz

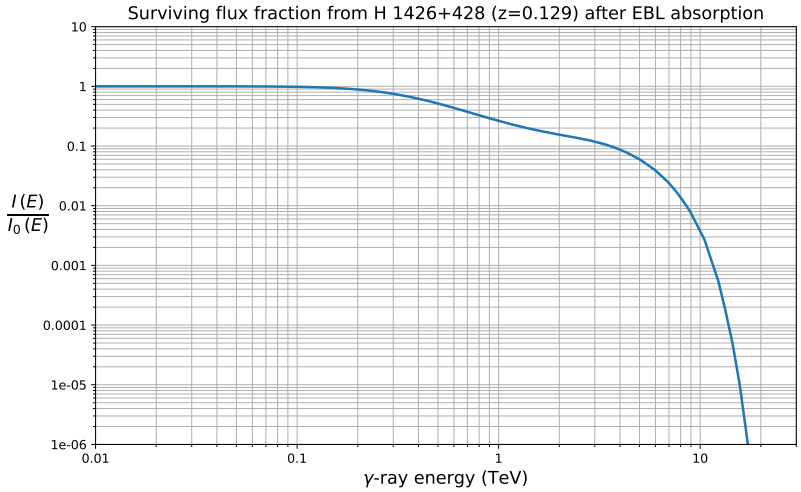

Figure 12: Surviving flux fraction from H 1426+428 (z=0.129) after EBL absorption made using the Francescini et al (2008) EBL model (using data from this work).

factors to the differential equation regarding the evolution of the electron energy distribution.

The package includes a module for each leptonic radiative process; synchrotron (with self-absorption) and inverse compton. The latter includes options to model either the same synchrotron photons produced in the former process (SSC, computed as in Finke et al. (2008)), or the external photons produced by the CMB etc (EIC). In both cases the full Compton cross-section is used, including the extreme Klein-Nishina regime.

AGNpy expands on science cases in packages such as Jetset or Naima, and is interfaceable with tools such as gammapy. It will be used in this thesis to model the SED of the blazar H 1426+428.

Chapter 3: Imaging Atmospheric Cherenkov Technique (IACT) and VERITAS

3.1 IACT

Space-based detectors such as Fermi-LAT [Atwood et al., 2009] can detect gamma-rays from distant sources at energies up to 300 GeV. For these types of detectors, a long exposure is required in order to detect low fluxes, due to the small effective area. Ground based telescopes can detect high energy gamma-ray sources quicker due to

their larger effective areas. Imaging Atmospheric Cherenkov telescopes are ground based and use the Earth's atmosphere as a key part of the detection technique. By using the Earth's atmosphere this way effective collection areas can exceed $10^5 m^2$.

This technique was first proposed by Jelly and Galbraith in the 1950s [Galbraith and Jelley, 1953], but separating the background presence of charged cosmic rays from gamma-ray events proved difficult. This issue was resolved by recording an image of the Cherenkov emission from the air showers using a matrix of photomultipliers in the focal plane to form the pixels of a digital camera. Only shower images that were the correct shape and whose axes were aligned with the target source would be accepted, and all others along with more complex images would be rejected.

The first detection of a TeV gamma-ray source was the Crab [Weekes et al., 1989], using the Whipple telescope in 1989 (see figure 13). A stereoscopic view could be provided by two such telescopes $\sim$ 100m apart, and this would allow study of low-energy showers also, as Cherenkov flashes produced by single muons passing close to one telescope could be rejected. The idea of the stereoscopic pair was then expanded to more modern arrays of more than four 10-15m telecopes, such as HEGRA [Aharonian and Heinzelmann, 1997], HESS, MAGIC, and VERITAS. The Cherenkov Telescope Array (CTA) [Acharya et al., 2017], when finished, will be the largest ground-based gamma-ray observatory in the world, with more than 100 telescopes in the northern and southern hemispheres. It will have unprecedented accuracy and will be 10 times more sensitive than existing instruments.

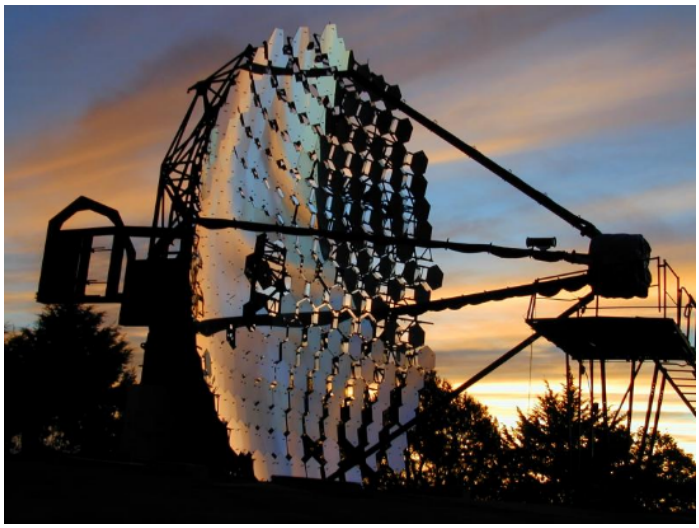

Figure 13: The Whipple telescope [Kildea et al., 2007]

When an incident high-energy gamma-ray or hadronic cosmic ray hits the Earth's atmosphere it will disappear in pair-production (see figure 14), a process in which a gamma-ray of sufficient energy will be converted into an electron and a positron. The electron and positron will keep their original trajectory and subsequent bremmstrahlung and pair-production interactions will lead to a particle shower, or cascade [Thompson, 2008]. The radiation length (the mean length (in cm) to reduce the energy of an electron by the factor 1/e), X_0 (37 grams/cm^2), for bremmstrahlung in the atmosphere (with atmospheric depth at sea level = 1000m) is close to the mean free path for pair production. This similarity is convenient in that we can make an approximation for the shower development [Heitler, 1984] in which the number of particles double every $2lnX_0$, and the primary gamma-ray energy, E_0, is split evenly among the secondary products. After the average electron energy drops to $E_c = 84$ MeV the shower will fall off, as this is the critical energy below which ionisation losses dominate. The maximum number of particles in the cascade is given by $\frac{E_0}{E_c}$ [Holder, 2021]. For a gamma-ray of 1 TeV, the shower reaches it's maximum of ~ 1000 charged particles roughly 8km above sea level, after which the energy is gradually absorbed by ionisation losses [Hillas, 2013]. Now detailed Monte Carlo simulations and Corsika [Heck et al., 1998] (a package used by VERITAS to simulate air showers) are used to reconstruct shower development.

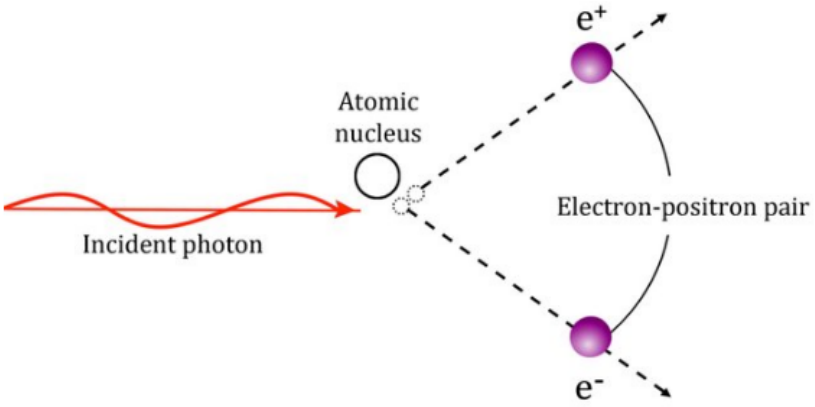

Figure 14: Pair production process [Omer and Hajima, 2018].

Relativistic charged particles in air showers will produce Cherenkov radiation, because they are moving faster than the speed of light in air. The maximum emission will come from the most particle-dense part of the shower. The particles will also be distributed over a small angular range due to multiple Coulomb scattering. This

Cherenkov radiation creates a pool of light on the ground which can be measured and extrapolated back in order to find the direction of the original gamma-rays. The observed angle of incidence (the Cherenkov angle) is important as it is used to compute the the direction and speed of a Cherenkov radiation-producing charge. The angle is zero at the threshold velocity for the emission of Cherenkov radiation. The shape and orientation of the shower is used to distinguish gamma-rays from hadronic cosmic rays, (which constitute the majority of air-showers), and to reconstruct the arrival direction and energy of the photon. Showers consisting of gamma-rays will have images that look like narrow, elongated ellipses, while cosmic ray shower images will look wider due to the emission angle of the pions, longer, and more irregular due to nearby penetrating particles.

The total Cherenkov yield from the shower is proportional to the energy of the primary particle (gamma-ray or cosmic ray). The primary energy can be estimated using the image intensity and the reconstructed distance of the shower core from each telescope. The lower energy threshold, E_T, at the trigger level will depend on: A, the photon collection efficiency, $\eta(\lambda)$, the Cherenkov light yield, $C(\lambda)$, the night sky background light, $B(\lambda)$, the solid angle, Ω, and the trigger resolving time, τ [Weekes, 2005].

$$E_T \propto \frac{1}{C(\lambda)} \sqrt{\frac{B(\lambda)\Omega_T}{\eta(\lambda)A}}$$

This function can be modified by the properties of the detector, and the elevation angle at which the observations are made.

3.2 VERITAS

VERITAS is an array of four 12m Cherenkov imaging telescopes located at the Fred Lawrence Whipple Observatory (FLWO) near Tucson in Arizona. It is used for gamma-ray astronomy in the $\sim$ 100 GeV – 30 TeV photon energy range, using the Imaging Atmospheric Cherenkov Telescope (IACT) technique, whereby gamma-rays that cause particle showers in the Earth's atmosphere are observed via the Cherenkov light produced. A view of the FLWO basecamp and the VERITAS array is shown in figure 15.

A VERITAS reflector consists of 350 identical hexagonal segmented mirrors (following the Davies-Cotton design [Davies and Cotton, 1957]) on steerable altitude-azimuth mounts, with a camera containing 499 photomultiplier tubes (designed to convert faint incoming light into an amplified electrical signal) at each mirror's focus. The multi-mirror design is advantageous over a single mirror, which would be expensive, heavy,

Figure 15: View of the FLWO basecamp and the VERITAS array. Credit: VERITAS Collaboration (veritas.sao.arizona.edu)

and difficult to maintain. Multiple, lighter mirrors make the positioning systems for the telescopes simpler [Holder et al., 2006].

The mirror reflectivity degrades over time due to exposure to the elements ($\sim$ 3 - 6 % of reflectivity at 320 nm is lost per telescope per year). To counter this, the mirrors are re-aluminised (the process by which aluminium vapours are diffused into the surface of the base metal, in this case creating a mirror), re-anodised (where the metal surface is converted into a more durable, corrosion resistant, anodic oxide finish), and washed regularly [Roache et al., 2008]. Due to a slow-down in the mirror re-aluminisation process the mirror reflectivity showed a continual decline in the 2012-2020 period, but this is accounted for using gain and throughput (GT) factors to update instrument response functions (IRFs) [Rosillo, 2021] for each observing year. IRFs are integral to data analysis with VERITAS in order to quantify the performance of the telescopes and connect estimated parameters with their true values.

Mirrors are aligned using the "raster" scan method [McCann et al., 2009], where a CCD camera is placed at the focal point of the reflector. The telescope will perform a scan of a star, and the camera will simultanously take a series of images of the reflector. The mirrors that are correctly aligned will appear bright when the telescope is pointing at the star, while the incorrectly aligned ones will appear bright when the angle between the star and the mirror is twice the misalignment angle of the mirror. The images are studied after the scan is finished and the improperly aligned mirrors can be corrected using the now known angle of misalignment.

Each camera is placed 12 metres from the mirrors in the focal plane of the telescope, and is stored in a "focus box" which is water tight and uses a rolling shutter system to protect the contents from the elements. Photomultiplier tubes are commonly used in ground based gamma ray astronomy due to their cost-effectiveness, fast response times

and large detection areas. They also produce a large signal-to-gain ratio for Cherenkov light, and are sensitive in the UV region of the electromagnetic spectrum [Wright, 2017]. To maximise light collection efficiency, VERITAS photomultiplier tubes are arranged in a hexagonal pattern. This will still leave small gaps between pixels where light is lost however, so the front of VERITAS cameras are fitted with a plate of 499 molded plastic "light cones" [Nagai et al., 2007] (see figure 16. These utilise a hybrid form of the Winston light concentrator design [Winston, 1970], which provides albedo protection (reduces background light incident on the PMT), and maximises the collection of incoming light over the desired field of view.

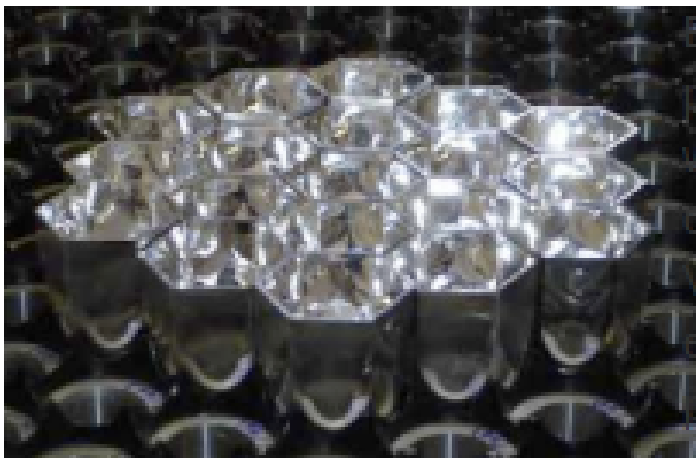

Figure 16: Some VERITAS lightcones [VERITAS homepage].

VERITAS has an energy range of 80 GeV to $>$ 30 TeV, with spectral reconstruction starting at 100 GeV. It has an energy resolution of 17% at 1 TeV, and a peak effective area of 100,000m^2 (See figure 17 and figure 18 for plots of angular resolution and effective area vs gamma-ray energy). VERITAS requires clear, dark skies in order to observe, with the moon less than half full - the observatory stops observing for approximately 6 days every month due to the brightness of the moon, and does not observe during monsoon season in the summer. Cherenkov telescopes have significantly reduced sensitivity and a higher energy threshold at below 60 degree elevation, for these reasons most VERITAS observations are limited to targets between +60 degrees and +90 degrees.

3.2.1 Trigger and data acquisition

In order to eliminate as many background events as possible, VERITAS operates on a three level trigger system: level one works on a single-pixel level, level two works

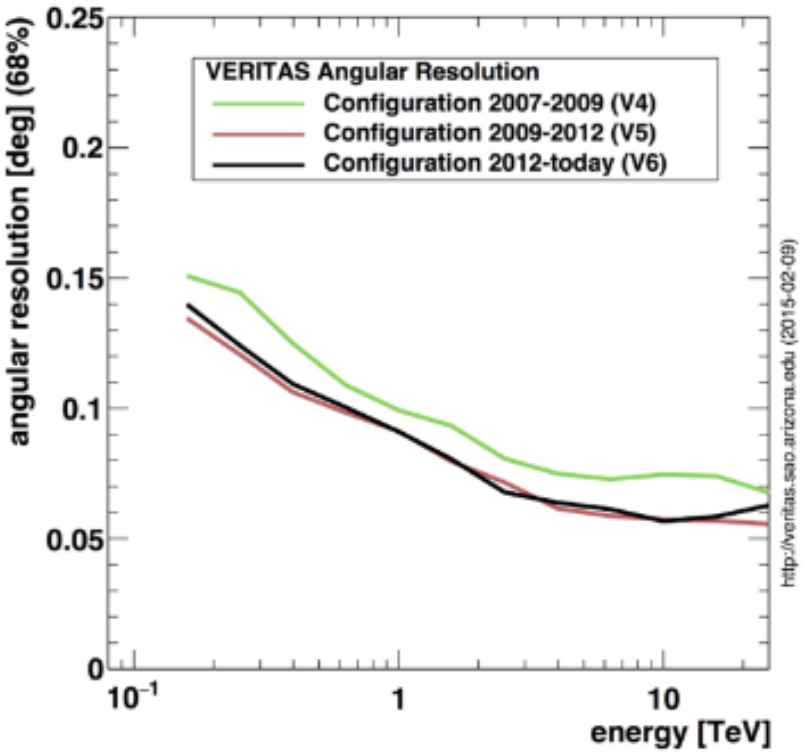

Figure 17: Angular resolution as a function of gamma-ray energy for VERITAS (elevation: 70 deg) [VERITAS homepage]

within a specific timing window to select specific patterns of single level pixels, and level three works on a array level, making sure that an air shower was detected by multiple telescopes.

As part of the level 1 trigger system, each PMT in the camera has a custom built constant fraction discriminator (CFD) and a threshold discriminator [Hall et al., 2003]. The output from a PMT is directed into the CFD, and if the sum of the voltages from the PMT pulse and a time-delayed copy cross a pre-defined threshold, an output logic pulse will be produced.

Level 2 is employed in order to reject night sky background (NSB) fluctuations and PMT after-pulsing. Cherenkov telescopes are particularly prone to these issues. Generally only one or two adjacent pixels at a time are affected by these fluctuations, so this issue is resolved by only triggering an output pulse when several adjacent pixels surpass the level one discriminator threshold (within some coincidence window).

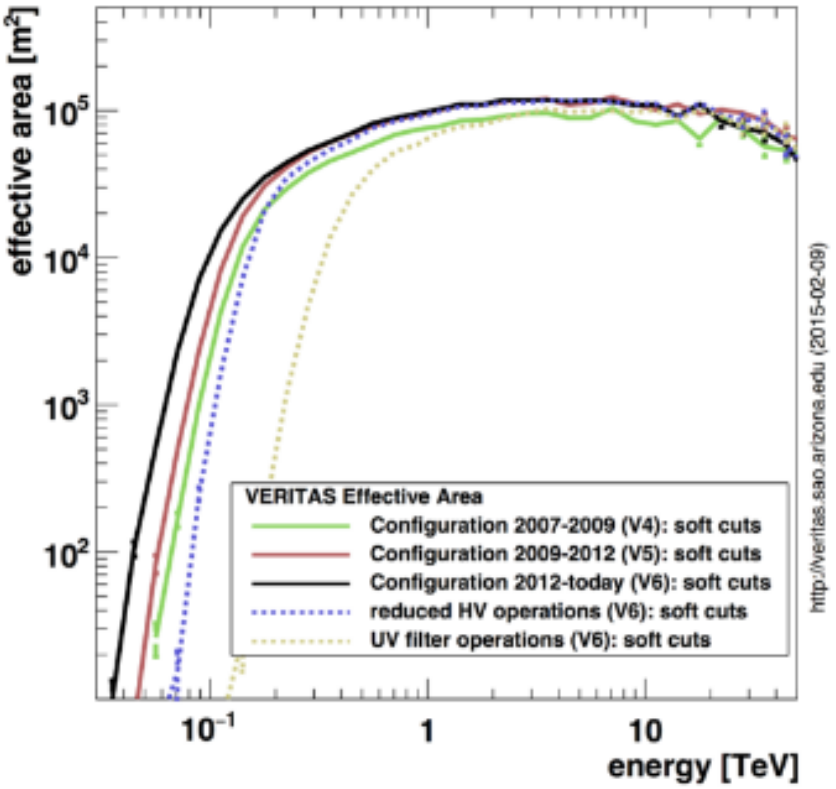

Figure 18: Effective area as a function of gamma-ray energy for VERITAS (elevation: 70 deg) [VERITAS homepage]

Local relativistic muons are a large source of background for Cherenkov telescopes at low energy. The images they create when they pass close by the telescope can be very similar to those from gamma-rays. The level 3 array-level trigger system effectively removes these background events, as the size of the Cherenkov cone produced by a muon means its detection will be limited to one telescope. Requiring triggers for more than one telescope in this way increases the gamma-ray sensitivity of the telescope, as the CFD thresholds can be lowered once single-telescope triggers by muons are removed [Weinstein, 2007].

The signal from the PMT is passed to an individual channel on the front-end of a flash Analog to Digital Converter (FADC) board [Rebillot et al., 2003]. This signal is then digitised at a sample rate of 500MHz, with each FADC providing an 8-bit dynamic range and 64 microsecond buffer-depth. When an air shower event is identified by the level 3 system, a logical signal is sent to each telescope which tells the telescope data

acquisition system to read out a section of this buffer for each PMT signal. Shape and timing information can be extracted from the high-resolution digitisation of the PMT signals provided by the FADC boards. The charge integration window per pixel can be minimised using the pulse rise-time and relative arrival time. This will improve the signal to noise ratio.

The FADC board signals will then be passed on to an event-building computer, where the complete events will be integrated, tested, and passed on to an array-level data harvester machine.

Clear skies and good weather are vital for VERITAS to observe. The temperature of the sky is monitored using three infrared pyrometers. Water vapour and droplets act as IR emitters, so a rise in sky temperature as measured by the pyrometers indicates the presence of water vapour/clouds. There is also a weather station which is equipped with a wind speed/direction sensor, a humidity sensor, a rainfall sensor, and a temperature sensor. If the wind is above speeds of 50kph, or humidity levels reach greater than 50 percent VERITAS does not operate in order to protect telescope mechanics and electronic systems. An optical monitor (in the form of a CCD camera) is fitted to each telescope to keep track of the telescope pointing and the night sky conditions in the FOV.

3.3 Data analysis

VERITAS data is stored in VERITAS bank format (VBF) files. These files store information such as the FADC traces for each pixel, event arrival times, number of participating telescopes, dead-time, array configuration etc. VERITAS collaboration members take data quality monitoring (DQM) shifts where the quality of the data is checked after each night of observing. VERITAS uses two data analysis packages, EventDisplay (ED), and VERITAS Gamma-ray Analysis Suite (VEGAS). The latter is the package used for this research. Generally results must be checked using each package separately to ensure consistency. VEGAS is written primarily in C++. A VEGAS analysis is done in stages:

3.3.1 Calibration:

VEGAS stage 1 calculates all hardware dependent quantities of the data including pixel, telescope, and array information. This stage is where bad pixels are identified, noise levels of the fluctuating NSB are calculated, and gain and timing parameters for each PMT are determined.

The first part of stage 1 is the calibration calculation, and involves the flasher run. Flashers are LED pulses that cycle through 6 or 8 different intensities, uniformly illuminating the camera at a fixed rate. They are taken each night for use in calibration. They can then be used to line up the timing between all pixels as well as to determine the sensitivity of each pixel compared to the rest of the camera.

The second part of stage 1 is the calibration application, and is run on the data to analyse the pedestal events (blank-sky readouts determining noise in each pixel) as well as retrieving necessary information from the database (e.g. tracking).

3.3.2 Image calibration, cleaning and parameterisation:

VEGAS stage 2 generates hardware independent parameterised events. Here the flasher info is combined with the data to produce calibrated files. Charge information for FADC traces (which are A/C coupled) for each channel is collected and the total charge in each pixel is calculated by integrating the traces. Pixels triggered by NSB fluctuations are eliminated using a simple cleaning algorithm. A pedestal variation (PedVar), which is the RMS of the noise in each pixel, is artificially triggered. Any pixels with signal-to-noise ratio ($\frac{integralcharge}{PedVar}$) exceeding 5 and any neighboring pixels with signal-to-noise ratio exceeding 2.5 are retained, and all others are discarded.

Hillas parameterisation [Hillas, 1985] (modelling the image as a 2D ellipse, see figure 19) is then performed on the calibrated, trace evaluated pixels. The Hillas parameters are intended to characterise the image of a gamma-ray shower on the camera plane with only a few quantities. As Hillas parameterisation is a moment analysis, it is low-cost computationally.

A newer method that can be used is the image template method (ITM), which is based on simulations of air showers (see below).

3.3.3 Shower parameterisation:

VEGAS stage 3/4 performs array-level reconstruction using lookup tables to construct the "mean-scaled" image shape parameters for comparison of the image with typical gamma rays. The energy is also calculated based on the lookup table. This is where shower direction, core location, height of the shower maximum, and gamma-ray energy of individual events are reconstructed at the array level. An image quality selection based on minimum number of pixels in an image, minimum image size, and maximum image distance is applied here also. This is used to exclude images that are

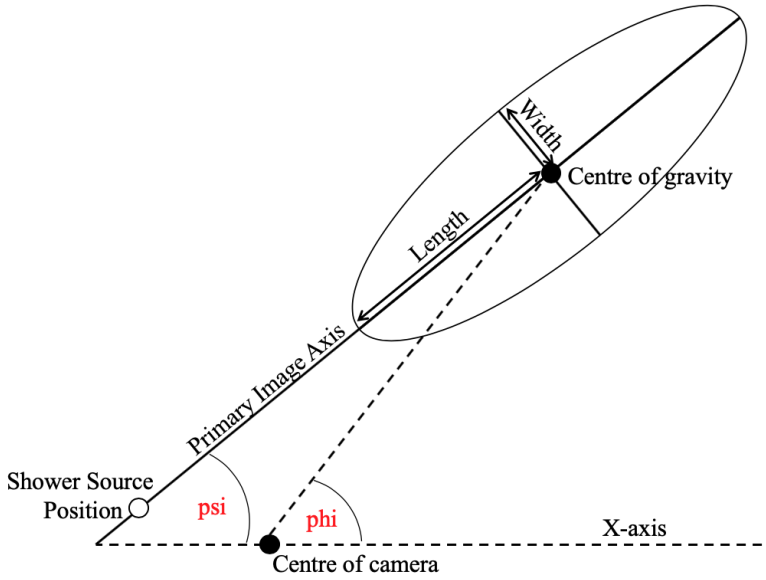

Figure 19: Hillas parameters

too faint, too small, or too close to the edge of the camera. Cuts will be applied at this stage based on the expected spectral shape of the observed source: soft, medium, and hard.

The shower core is defined as the location where the gamma-ray would have hit the ground in the absence of the atmosphere, and is calculated by determining the intersection of the major axes of each image in the ground plane. The arrival direction of the primary particle, the shower direction, is determined similarly to the shower core - by calculating where the major axes from all participating telescopes overlap. The impact parameter is the distance between the core location and any given telescope. The shower maximum is the height at which the most Cherenkov light is produced, and this can be calculated using the impact parameter. The shower maximum is particularly useful in separating gamma-rays from cosmic rays, as the latter tend to penetrate further into the atmosphere before interacting with other particles.

The size and the impact parameter can be used to determine the energy of each event. These parameters are stored in lookup tables generated using simulations of gamma-ray showers for a wide range of observing parameters. The weighted average of each energy is used for the event.

3.3.4 Gamma-hadron separation:

VEGAS stage 5 takes output from stage 3 (Hillas parameterisation) and stage 4 (stereo reconstruction) and applies cuts for background rejection (performs the gamma/hadron separation). Time cuts may also be applied here (in the case of a run taken during bad weather, for example).

Electromagnetic and hadronic initiated showers propagate differently through the atmosphere, and their geometries can be used to separate them. Observed shower properties are compared to simulated ones in order to determine which are gamma-rays and which are cosmic rays. Mean scaled width (MSW) and mean scaled length (MSL) (both calculated in stage 4) are used in stage 5 to determine how gamma-like the shower is.

$$MSW = \frac{1}{N_{images}} \sum_{i=1}^{N_{images}} \frac{width_i}{width_{sim}}(\theta_i, r_i, size_i)$$

$$MSL = \frac{1}{N_{images}} \sum_{i=1}^{N_{images}} \frac{length_i}{length_{sim}}(\theta_i, r_i, size_i)$$

$Length_{sim}$ and $width_{sim}$ are the average lengths and widths for the simulated gamma ray images with zenith angle θ, $size$, and impact distance r. MSL and MSW values closest to 1.0 will be most likely to be gamma-rays. Distributions of mean scaled length and width for gamma-initiated showers and hadron-initiated showers are compared in figure 20.

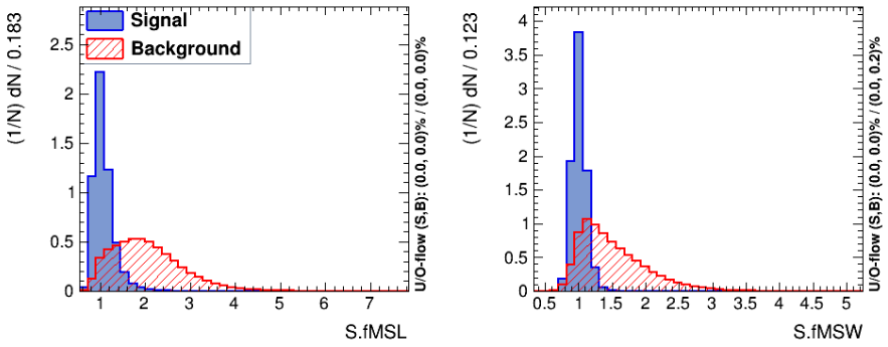

Figure 20: Left: the distributions of mean scaled length are compared between gamma-initiated showers in blue and hadron-initiated showers in red. Right: the same distributions for mean scaled width [Petrashyk, 2019]

3.3.5 Results extraction:

Stage 6 determines the significance of the observations, skymaps, results, and spectrum. It requires effective area files.

Despite the gamma-hadron separation steps, there will still be cosmic rays that slip through. The first step is removing this background by defining an ON and an OFF region: ON being the region of scientific interest (the target) and OFF being the background. VERITAS observes the ON and OFF regions in the same field of view at the same time.

Two methods for forming an OFF region are used. In the reflected region method (also called a wobble analysis), the source is offset by 0.5 degrees from the telescope tracking position, and OFF regions consist of regions of the same size as the ON region with the same offset. This allows for both on-source observations and simultaneous estimation of the background contamination caused by charged cosmic rays, which will reduce the uncertainties involved in using separate pointings for background estimation. In the ring background method (RBM) the OFF region is an annulus surrounding the ON region [Archambault et al., 2017b]. α is defined as the ratio of exposure in the ON region to that in the OFF region, and N_{excess} is defined below. An illustration of the ring background method vs the reflected region method is presented in figure 21.

$$N_{excess} = N_{ON} - \alpha N_{OFF}$$

We can then define the statistical significance of a source in the ON region as follows, using equation 17 in Li and Ma (1983).

$$S = \sqrt{2}\left(N_{ON} ln\left[\frac{1+\alpha}{\alpha}\frac{N_{ON}}{N_{ON}+N_{OFF}}\right] + N_{OFF} ln\left[(1+\alpha)\frac{N_{OFF}}{N_{ON}+N_{OFF}}\right]\right)^{\frac{1}{2}}$$

Spectral reconstruction and flux calculation are then performed using a binned approach. For this, the effective area of the instrument, the live time, and N_{excess} are required. Effective area files (as a function of zenith angle, NSB noise level, season and analysis cuts) are created using Monte Carlo simulations of the air showers. The default source spectral shape is assumed to be a power law ($\frac{dN}{dE} = N_0(\frac{E}{0})^{-\gamma}$) in VEGAS, but there are options for log parabola, exponential cutoff power law and others.

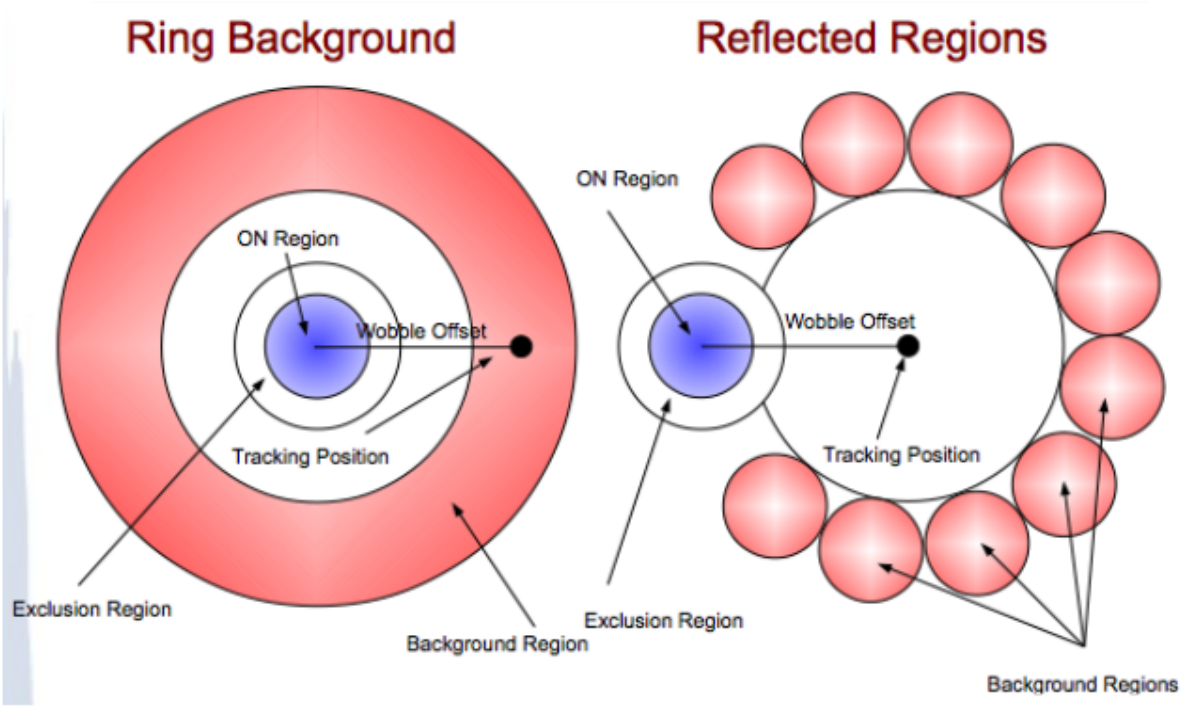

Figure 21: RBM analysis (left) vs wobble/reflected region analysis (right). The ring size is defined in the stage 6 analysis options.

3.3.6 Image template method:

The image template method uses templates that are based on simulations of showers as a function of energy, zenith angle, core location and depth of first interaction in the atmosphere (see figure 22). These templates store predictions of the average photoelectrons, and these are compared to observed values, and the likelihood can then be calculated in order to find the optimum gamma-ray parameters.

The ITM method is more accurate than the standard VEGAS analysis, which relies on the weighted average of the axis of elongation in the images to determine the gamma-ray direction, and on lookup tables that relate the predicted energy to the observed energy. The ITM method is also not biased by missing pixel information due to pixel cleaning, or the edge of the camera. It does, however, require more CPU space and therefore takes longer to run. The ITM method was used for this project.

The VEGAS analysis chain with a summary of each stage along with execution times is presented in table 1.

Stage	Purpose	Input(s)	Output	Time(m)	Size(MB)
1	Calib. Calculation	Raw Data	Calibration Data	8.2	51
2	Calib. Application	Raw + Calibration Data	Calibrated Events	39	6200
3	Image Param.	Calibrated Events	Param'd Events	14	224
4	Shower Recon	Param'd Events	Recon'd Showers	6	40
5	Event Selection	Recon'd Showers	Selected Events	< 2	202
6	Results	Selected Events	Statistics & Figures	< 1	< 1

Table 1: The VEGAS analysis chain with execution time [Cogan, 2007].

Chapter 4: VERITAS analysis of H 1426+428

H 1426+428 has been a long-term target for VERITAS observations due to the potential to study the physics of hard-spectrum blazars and to constrain the extragalactic background light. It was detected by the previous generation of imaging atmospheric Cherenkov telescopes, Whipple [Horan et al., 2002], and HEGRA [Aharonian et al., 2002] at flux levels up to 80% of the Crab Nebula flux, with a redshift of z=0.129. Based on initial observations by VERITAS between 2008 and 2010 which indicated that H 1426+428 was in a low-flux state of approximately 2% of the Crab [Benbow, 2011], it was decided to attempt to take multiple exposures each observing season to search for elevated states which would motivate Target-of-Opportunity (ToO) observations, and to build statistics for its low-state spectrum. No significant flaring activity was found after eight years of monitoring (2008-2016) with the data analysed by an automatic next-day analysis suite. The VERITAS Collaboration decided to produce a paper incorporating VERITAS data and multi-wavelength data from other telescopes, and to construct and model its broadband low-state SED.

Every VERITAS publication requires that the data be analysed by two independent analysis packages (called primary and secondary analyses) and the secondary analysis that I performed for the 2008-2016 paper are presented in this chapter. VERITAS continued to take data annually on H 1426+428 and in 2021 the VERITAS next-day analysis package revealed an increased H1426+428 flux compared to previous measurements [Quinn and VERITAS Collaboration, 2021], which prompted intensive VERITAS and multi-wavelength observations. A VERITAS paper describing the 2021 observations is also currently in production, and the secondary analysis that I performed on this VERITAS data is also presented in this chapter.

The primary and secondary analyses have been found to agree very well. Both papers are in advanced stages of preparation and will be submitted in the next few months.

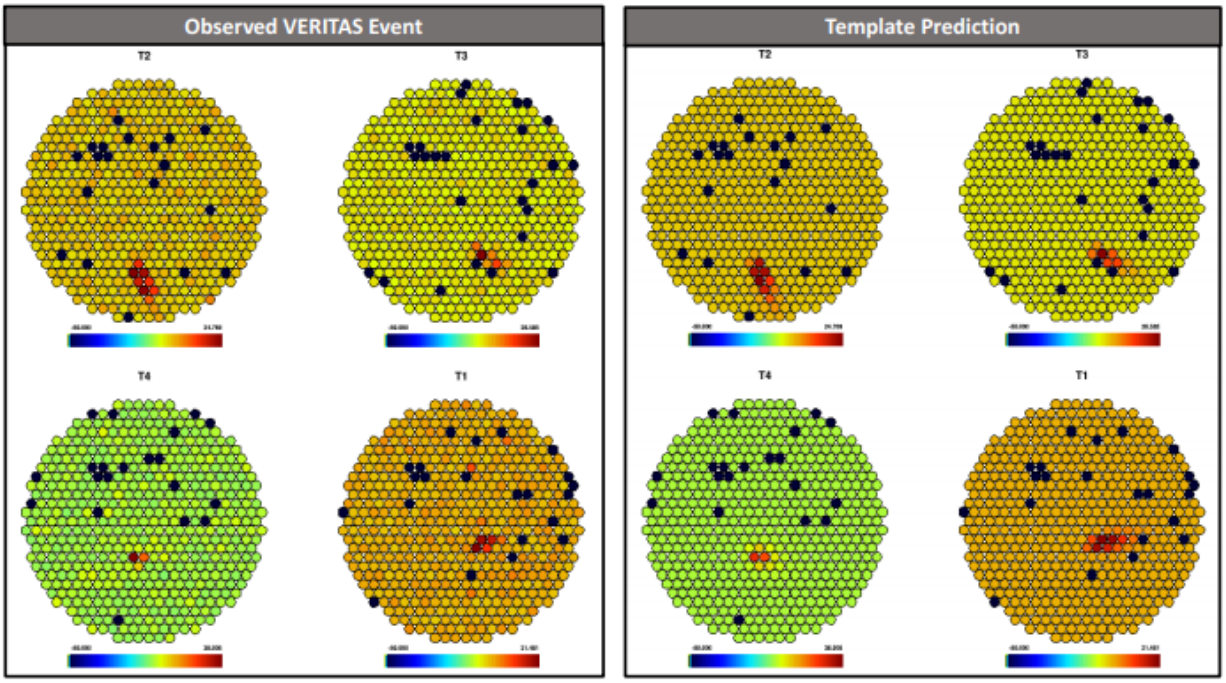

Figure 22: : Images from each of the four VERITAS telescopes. (left) Real candidate γ-ray event, (right) Image-template prediction [Christiansen, 2017].

4.1 Observations

VERITAS began targeting H 1426+428 in a coordinated fashion in the 2008-2009 observing season with the strategy guided by initial observational results. Typically 10-30 hours each season were requested but different exposures were achieved due to different observing priorities as well as weather conditions. In particular, observations of H 1426+428 during the 2012-2013 observing season were severely impacted by ToO observations on another object. VERITAS also made some observations during bright moonlight using reduced high voltages and ultra-violet filters [Archambault et al., 2017a], and at low-zenith angles. These are not included in the analysis in this thesis nor in the upcoming publications due to lack of corresponding IRFs for these types of runs.

Table 2 describes the VERITAS data set on H 1426+428 since 2008 analysed in this thesis and lists the number of observation runs, total exposures and exposures post data quality monitoring (DQM - see chapter 3) assessment, excluding runs that were outside the range covered by the available IRFs. In total 416 observing runs with a total exposure of 175 hours were assessed with runs either accepted, accepted with

Table 2: VERITAS observations of H 1426+428 analysed in this work

Observing Season	# Observations	Total Exposure (hrs)	Accepted for Analysis (hrs)
2008-2009	6	2	1.6
2009-2010	43	14	7
2010-2011	40	13	6.9
2011-2012	64	21	17
2012-2013	10	4	1.6
2013-2014	67	33	22.4
2014-2015	51	22	18.5
2015-2016	39	18	15.9
2020-2021	96	48	35.8

Table 3: Medium cuts ITM

ON region	MSW lower	MSW upper	MSL lower	MSL upper
0.070711 degrees	0.05	1.1	0.05	1.3

time cuts, or rejected. The resulting total good exposure for analysis was 126.7 hrs.

The data were all analysed using the VEGAS ITM analysis as described in chapter 3. The 2008-2016 and 2021 data sets are analysed and presented separately. The 2008-2016 exposure after livetime correction is 90.9 hours, while the 2021 data set after livetime correction is 35.8 hrs.

4.2 Analysis of the H 1426+428 2008-2016 data set

First the complete data set from 2008-2016 were combined and analysed together using the wobble analysis (see chapter 3) method to test for a clear detection of the source and to derive a time-averaged spectrum. The ring-background method (see chapter 3) was used to generate sky maps to check for the presence of artefacts such as holes caused by bright stars or additional excesses (which would indicate more exclusion regions were needed in the analysis), and that the source was in the correct location. Once the overall spectrum had been derived, an investigation was then conducted on the flux variability by producing light curves on three different timescales: yearly, monthly and daily.

For this analysis point source medium cuts ITM was used. The cuts used are shown in table 3.

Table 4: Wobble analysis results 2008-2016

exposure time	ON	OFF	eff alpha	significance	background rate
4412.83	968	7294	0.07	16.8	0.12 counts/s

4.2.1 Source detection (2008-2016)

The results of the wobble analysis for the detection of a source at the known location of H 1426+428 are shown in table 4. Because the wobble analysis uses four different pointing directions which have different stars in the field of view, the exclusion regions in each field are different and hence so is the alpha value (alpha is the ratio of the on to off regions - see chapter 3). The effective alpha is given in the table, however in the actual calculation of the significance the modified Li & Ma formula with a weighted alpha is used [Li and Ma, 1983] (see section 3.3.5).

The significance sky map is shown in figure 23 and the distributions of significances in the sky maps are shown in figure 24. Stars with B magnitude less than 8 were excluded with an exclusion region of radius 0.15 deg. per star. The ring size is the angular size of the regions used in the reflected region model (this value is the square root of the quantity often referred to as theta squared); this was set to 0.070711. The squared angular radius of the ON-source searching window was set to 0.005 degrees.

The significance sky map indicates a clear excess at the location of H 1426+428 with no additional sources present. To investigate whether the background variations in the sky map are statistical as would be expected, the significance distributions for all bins, all bins minus source exclusion, all bins minus star exclusion, and all bins minus all exclusions are plotted in figure 24. Stars cause holes (deficits) in the sky maps while additional sources show up as excesses. As can be seen from the significance distributions, there is a clear excess due to the source which disappears when the source is excluded and there are no deficits due to unaccounted-for stars. The final significance distribution (bottom right) with both source and star exclusions looks statistical and gives confidence in the analysis and source location of maximum significance.

The analysis resulted in 968 ON counts, 7294 OFF counts, an effective alpha of 0.04, a significance of 16.77, and a background rate of 0.12 (as summarised in table 4).

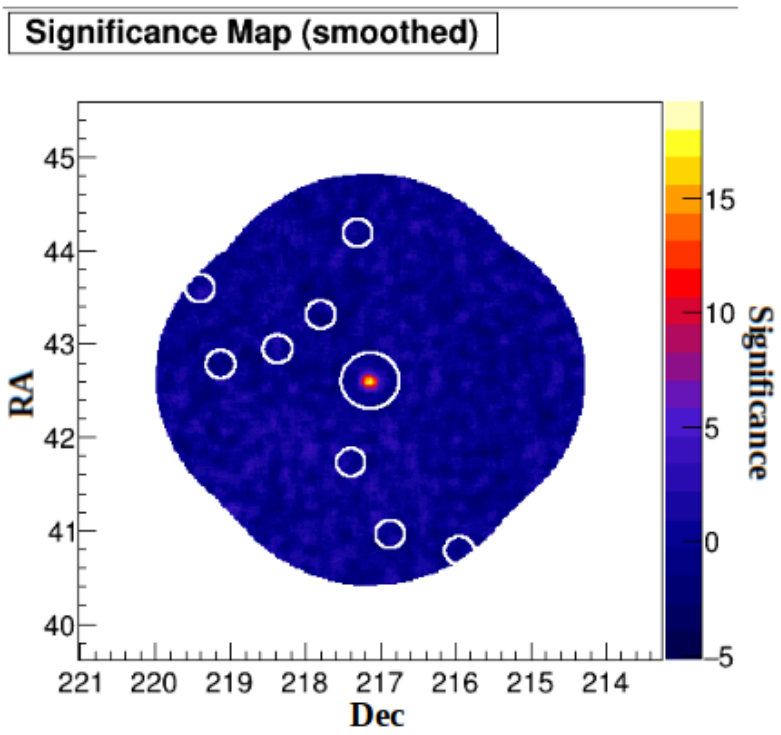

Figure 23: H 1426+428 2008-2016 significance map. The white circles denote the positions of stars.

4.2.2 VHE Spectrum (2008-2016)

The 2008-2016 H 1426+428 time-averaged spectrum from VERITAS was produced using the wobble analysis as described in chapter 3 and using the appropriate effective area lookup table for each run. Lookup tables and effective areas were selected for each run automatically using a python script that I contributed to (see appendix). The energy threshold was set at 0.25 TeV and the spectrum was binned in equal logarithmically spaced bins with Δlog10 E = 0.2. Only spectral points which have positive significances and positive excess events (> 0.5 for both) are included in the fit. It was found that there are 6 spectral bins with detections and these are shown in table 5 and figure 25. The plus signs in front of the bin numbers in table 5 indicate positive detections. The 'sig' column shows the significance of each bin calculated according to equation 17 of Li and Ma [1983], modified to take account of combining runs with different alpha values [Aharonian et al., 2004]. The low edge and high edge columns show lower bin edge and higher bin edge in TeV, respectively. Energy is given in TeV and flux in erg cm^{-2} s^{-1}.

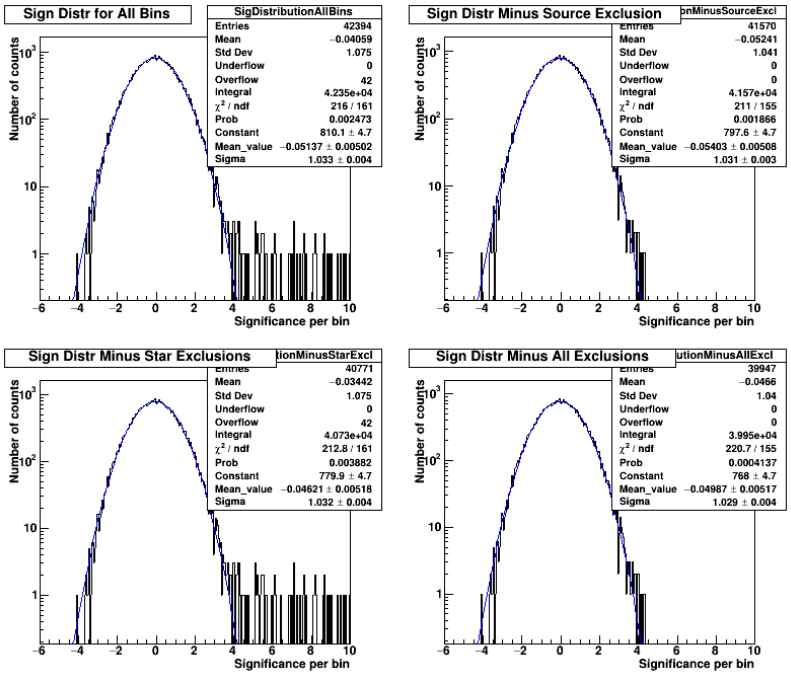

Figure 24: H 1426+428 2008-2016 significance distributions. Top right is the significance distribution for all bins, Top left is the significance distribution for all bins minus source exclusion, bottom right is the significance distribution for all bins minus star exclusions, and bottom left is the significance distribution for all bins minus all exclusions.

It was found that the first model used, a power law as described by equation $\frac{dN}{dE} = N_0 \left(\frac{E}{1\ \mathrm{TeV}}\right)^{-\Gamma}$, gave a satisfactory fit (with $\chi^2/dof = 0.46/4$). The energy bins and spectral flux densities are given in table 5, the best-fit parameters are given in table 6, and the best-fit spectrum is plotted over the spectral points in figure 25. The spectral index was found to be -2.6 ± 0.1, which is harder than that in the original Whipple [Horan et al., 2002] and HEGRA detections [Aharonian et al., 2002]. The resulting integral flux above 0.25 TeV is $(2.6 \pm 0.2) \times 10^{-8}$ photons m^{-2} s^{-1} which corresponds to a flux of $\sim 1.5\%$ Crab, indicating that H1426+428 is in a much lower flux state than when it was originally detected by Whipple [Horan et al., 2002] and HEGRA [Aharonian et al., 2002].

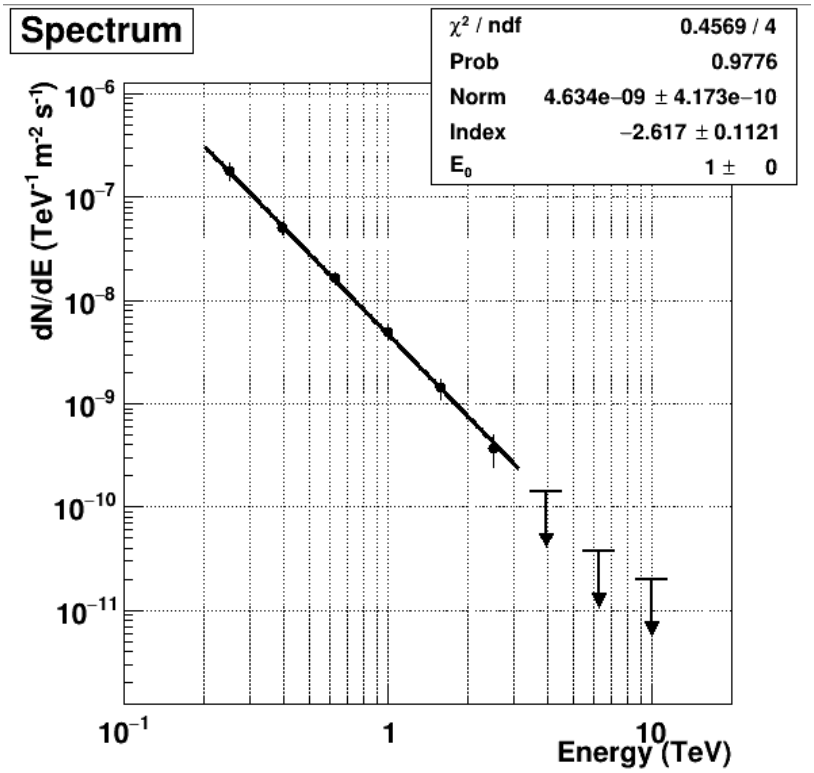

Figure 25: H 1426+428 2008-2016 spectrum

Bin	Energy	Flux	error	Non	Noff	Nexcess	RawOff	Alpha	Sig	Low Edge	High Edge
+1	0.2498	1.78e-07	3.45e-08	299	185.35	113.65	2608.00	0.07107	7.36	0.1995	0.3162
+2	0.396	4.98e-08	6.91e-09	233	112.94	120.06	1590.00	0.07103	9.44	0.3162	0.5012
+3	0.6275	1.63e-08	2.27e-09	148	58.18	89.82	819.00	0.07103	9.37	0.5012	0.7943
+4	0.9946	4.93e-09	8.32e-10	92	33.88	58.12	477.00	0.07103	7.82	0.7943	1.2589
+5	1.576	1.42e-09	3.24e-10	48	16.84	31.16	237.00	0.07103	5.88	1.2589	1.9953
+6	2.498	3.72e-10	1.28e-10	21	7.46	13.54	105.00	0.07103	3.85	1.9953	3.1623
7	3.96	1.43e-10	-1	5	5.26	-0.26	74.00	0.07103	-0.11	3.1623	5.0119

Table 5: H 1426+428 2008-2016 spectral results: The low edge and high edge columns show lower bin edge and higher bin edge in TeV, respectively. Energy (bin centre) is given in TeV and flux in erg cm^{-2} s^{-1}.

Table 6: Summary of 2008-2016 spectral analysis

Norm	Index	Integral flux > 0.25 TeV
$(4.6 \pm 0.4) \times 10^{-9}$ TeV^{-1} m^{-2} s^{-1}	-2.6 ± 0.1	$(2.6 \pm 0.2) \times 10^{-8}$ photons m^{-2} s^{-}1

Since H 1426+428 is at a redshift of z=0.129, absorption of VHE photons by the extragalactic background light will soften the very high energy spectrum. Using the model of Franceschini et al. [2008] as provided in the Gammapy package [Lefaucheur et al., 2020], the EBL attenuation factors have been calculated and are used to de-absorb the spectral points (see appendix). The tau and absorption factors for each of the spectral bins for an object at z=0.129 are shown in table 7 and the absorbed and de-absorbed spectral energy density (E^2 dN/dE) points are shown in figure 26. The de-absorbed spectrum shows no indication of a turn over and the peak in the inverse-Compton component looks to be above 2.5 TeV.

Table 7: Energy, tau and $e^{-\tau}$ values

E	τ	$e^{-\tau}$
0.250	0.199	0.819
0.396	0.469	0.625
0.628	0.875	0.417
0.995	1.324	0.266
1.576	1.705	0.182
2.498	2.002	0.135
3.960	2.428	0.0882
6.275	3.379	0.0341
9.946	5.549	0.00389
15.760	11.587	9.28×10^{-6}
24.980	30.081	8.63×10^{-14}

4.2.3 Flux Variability (2008-2016)

To search for flux variability the data were binned on different timescales and the spectrum fit with a power law with index fixed to the index from the overall data set

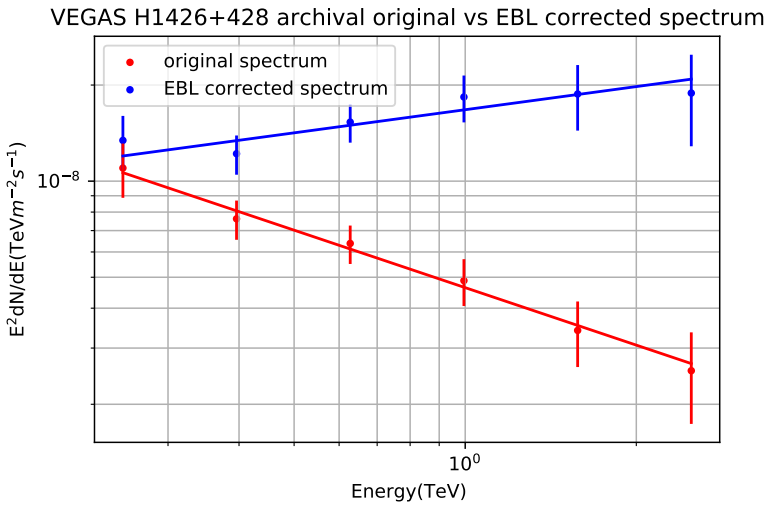

Figure 26: H 1426+428 archival original vs EBL corrected spectrum, plotted in E^2dNdE

Table 8: Chi squared analysis of lightcurves 2008-2016

Timescale	Chi-squared	p-value	DoF
Nightly	35.299	0.81	77
Monthly	33.193	0.19	27
Yearly	35.299	1×10^{-5}	7

but with the normalisation constant allowed to vary. The integral flux and error were then determined. The timescales investigated were yearly, monthly and daily. Each timescale was analysed for variability by calculating the χ^2 value and probability for constant flux. Light curves were produced using macros that I developed which divide run lists according to the timescale desired, run analyses on each group of runs and plot the resultant fluxes against MJD (see appendix).

The light curves are shown in 27 and the results of the chi squared analysis in table 8. The results show that there were clearly no significant flaring episodes detected in the VERITAS data. The chi-square values indicate no/low-level of variability on monthly and nightly timescales, with some evidence of variability from year to year.

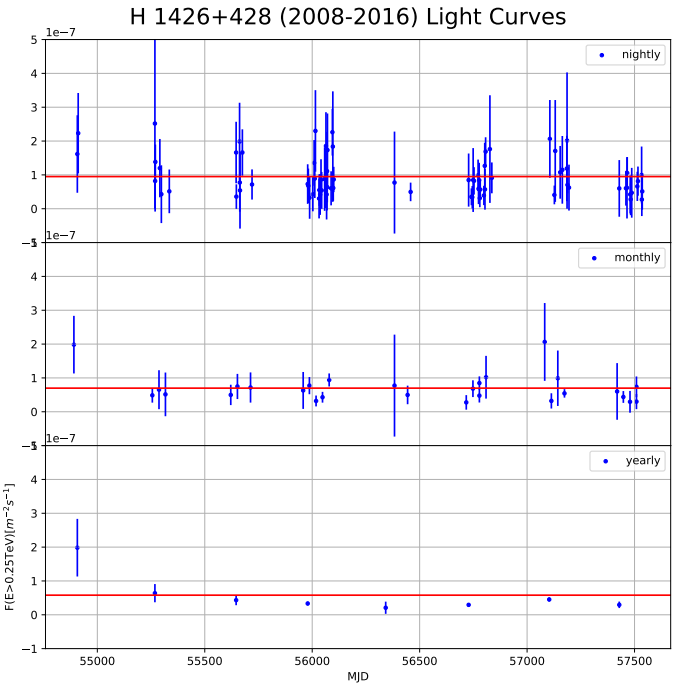

Figure 27: H 1426+428 2008-2016 nightly, monthly and yearly light curves, with the horizontal red lines corresponding to the mean flux values

4.3 Analysis of the 2021 H 1426+428 data set

35.8 hours of 2021 data spanning 3 months were analysed using VEGAS. Again, runs with low zenith angles and reduced high voltage were removed and wobble and ring background methods were used. There were 478 ON counts and 2051 OFF counts. The effective alpha was 0.07 and the detection significance was 20.54, with a background rate of 0.08 (as summarised in table 8).

Point-source medium cuts ITM was used again. The cuts used are shown in table 3.

4.3.1 Source detection (2021)

The results of the 2021 data wobble analysis for the detection of a source at the known location of H 1426+428 are shown in table 9. The significance sky map is shown in figure 28 and the distributions of significances in the sky maps are shown in figure 29. Again, stars with B magnitude less than 8 were excluded with an exclusion

Table 9: Wobble analysis results 2021

exposure time	ON	OFF	eff alpha	significance	background rate
1827.93	478	2051	0.07	20.54	0.08 counts/s

region of radius 0.15 deg. per star. The significance sky map for the 2021 data also indicates a clear excess at the location of H 1426+428 with no additional sources present. The significance distributions plotted in figure 29 clearly show an excess due to the source which disappears when the source is excluded, with no deficits due to unaccounted-for stars. The final significance distribution (bottom right) with both source and star exclusions also looks statistical and gives confidence in the analysis and source location of maximum significance.

The analysis resulted in 478 ON counts, 2051 OFF counts, an effective alpha of 0.07, a significance of 20.54, and a background rate of 0.08 (as summarised in table 7).

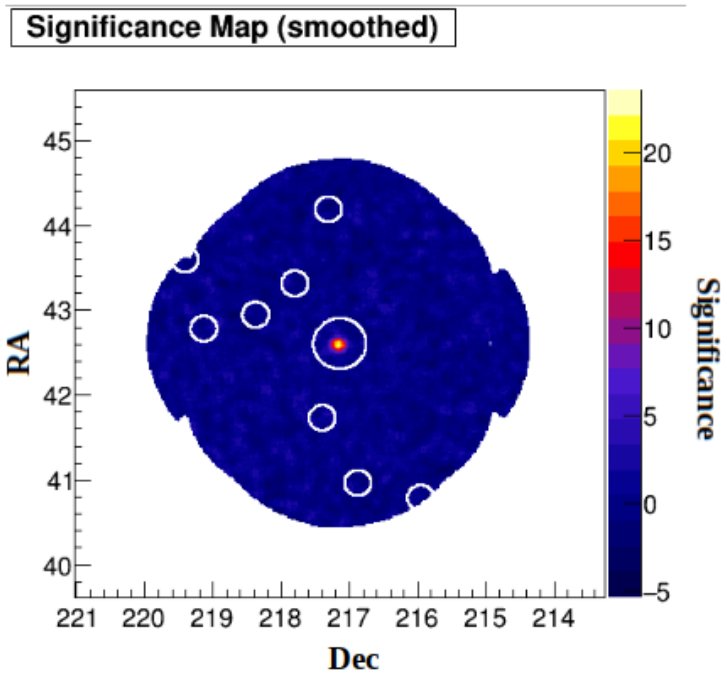

Figure 28: H 1426+428 2021 significance map

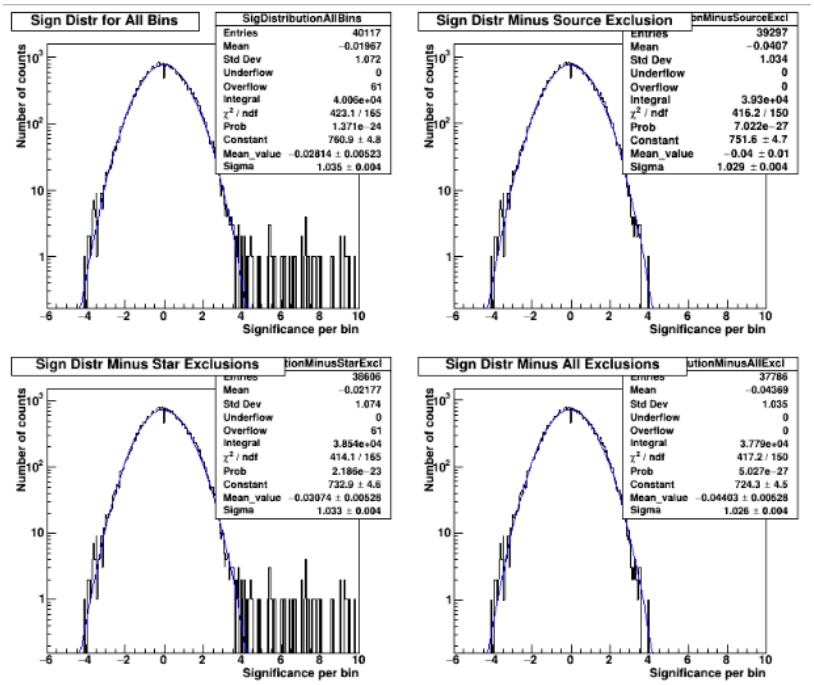

Figure 29: H 1426+428 2021 significance distribution

4.3.2 VHE Spectrum (2021)

The 2021 H 1426+428 time-averaged spectrum from VERITAS was produced using the same method as the 2008-2016 spectrum. It was found that the source was detected up to 6 TeV and there are 8 spectral bins with detections. These are shown in table 4.3.2 and figure 30.

It was found again that a power law gave a satisfactory fit (with $\chi^2/dof = 5.817/6$). The best-fit parameters are given in table 10, the energy bins and spectral flux densities are given in table 4.3.2 and the best-fit spectrum is plotted over the spectral points in figure 30. The spectral index was found to be -2.7 ± 0.1. The resulting integral flux above 0.25 TeV is $(2.7 \pm 0.2) \times 10^{-8}$ photons m^{-2} s^{-1} which corresponds to a flux of $\sim 1.6\%$ Crab.

Table 10: Summary of 2021 spectral analysis

Norm	Index	Integral flux > 0.25 TeV
$(8.3 \pm 0.6) \times 10^{-8}$ TeV^{-1} m^{-2} s^{-1}	-2.7 ± 0.09	$(4.6 \pm 0.3) \times 10^{-8}$ photons m^{-2} s^{-1}

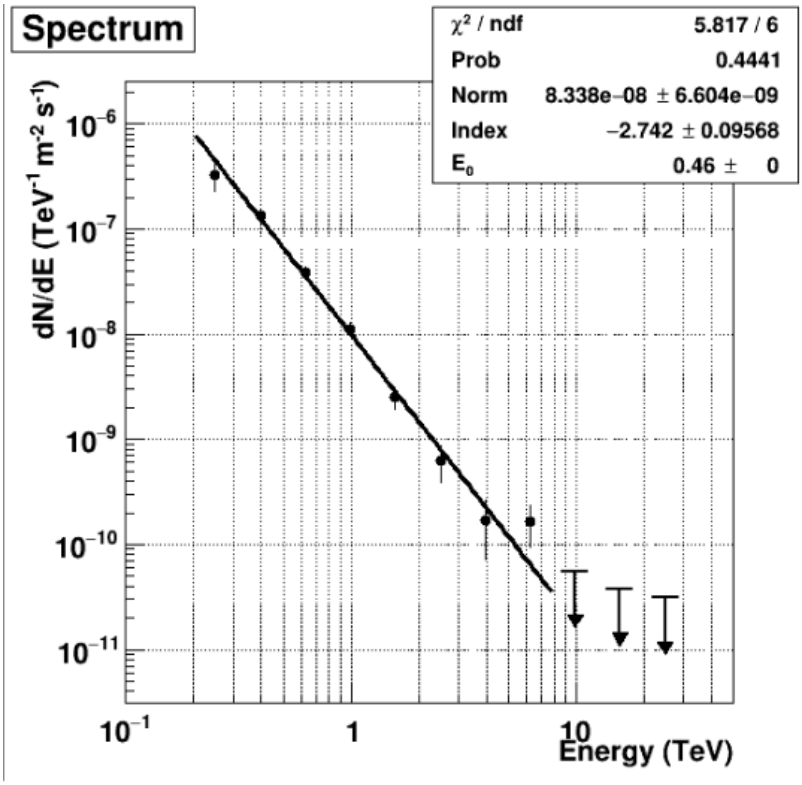

Figure 30: H 1426+428 2021 spectrum

The spectral analysis resulted in an integral flux (above 0.25TeV) of $(4.6 \pm 0.3) \times 10^{-8}$ and a spectral index of -2.7 (softer than the 2008-2016 analysis spectral index of -2.6, but both still agree within errors).

The EBL attenuation factors for H 1426+428 have been calculated again for the 2021 data and are used to de-absorb the spectral points. The tau and absorption factors for each of the spectral bins for an object at z=0.129 are shown in table 7. The absorbed and de-absorbed spectral energy density (E^2 dN/dE) points are shown in

Bin	Energy	Flux	error	Non	Noff	Nexcess	RawOff	Alpha	Sig	Low Edge	High Edge
+ 1	0.2496	3.26e-07	9.6e-08	57	26.59	30.41	368.00	0.07224	4.88	0.1995	0.3162
+ 2	0.3955	1.34e-07	1.67e-08	149	42.24	106.76	593.00	0.07123	12.05	0.3162	0.5012
+ 3	0.6269	3.82e-08	4.87e-09	106	24.00	82.00	337.00	0.07123	11.56	0.5012	0.7943
+ 4	0.9935	1.12e-08	1.7e-09	67	12.32	54.68	173.00	0.07123	10.14	0.7943	1.2589
+ 5	1.575	2.5e-09	5.93e-10	30	6.77	23.23	95.00	0.07123	6.16	1.2589	1.9953
+ 6	2.496	6.33e-10	2.4e-10	14	4.13	9.87	58.00	0.07123	3.60	1.9953	3.1623
+ 7	3.955	1.69e-10	9.65e-11	6	1.57	4.43	22.00	0.07123	2.54	3.1623	5.0119
+ 8	6.269	1.64e-10	6.93e-11	8	1.21	6.79	17.00	0.07123	3.79	5.0119	7.9433
9	9.935	5.57e-11	-1	0	0.57	-0.57	8.00	0.07123	-0.75	7.9433	12.5893

Table 11: H 1426+428 2021 spectral results: The low edge and high edge columns show lower bin edge and higher bin edge in TeV, respectively. Energy (bin centre) is given in TeV and flux in erg cm^{-2} s^{-1}.

figure 31. The de-absorbed spectrum again shows no indication of a turn over and the peak in the inverse-Compton component looks to be above 2.5 TeV.

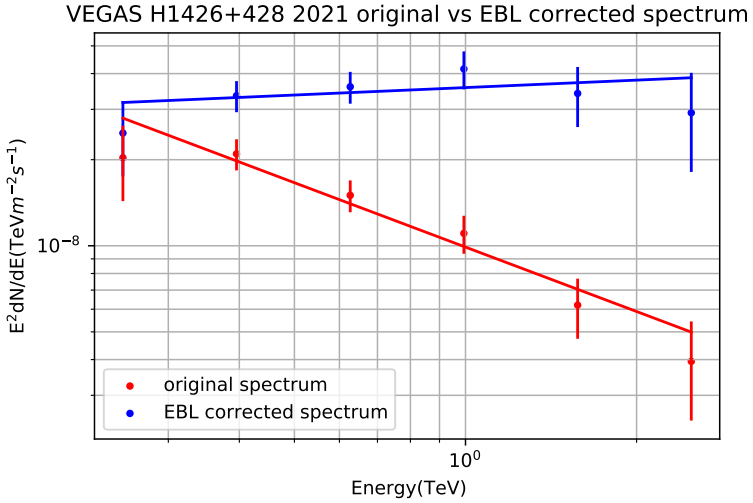

Figure 31: H 1426+428 2021 original vs EBL corrected spectrum

4.3.3 Flux Variability (2021)

To investigate flux variability the spectrum was again fit with a power law with index fixed to the index from the overall data set but with the normalisation constant allowed to vary. The integral flux and error were then determined. As the 2021 data comprised just 3 months of observations, only a nightly light curve was produced and

then analysed by calculating a the χ^2 value and probability for constant flux.

The light curve is shown in figure 32. The chi-square value (51.6, with p-value of 0.0002 and 21 degrees of freedom) again indicates no/a low-level of variability on a nightly timescale.

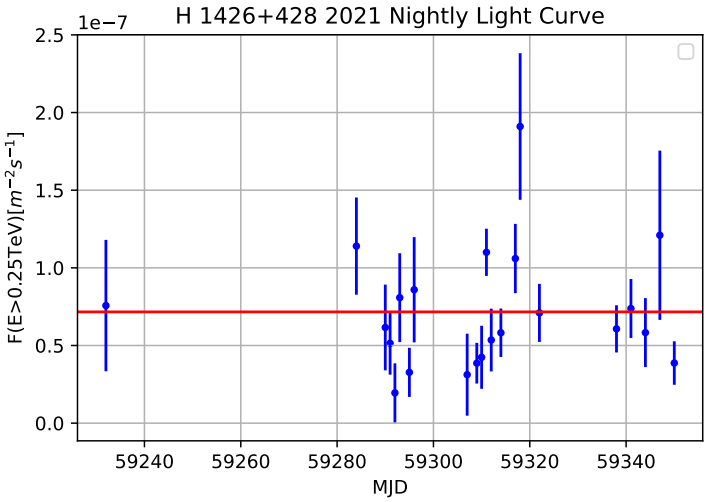

Figure 32: H 1426+428 2021 nightly lightcurve, with the horizontal red line corresponding to the mean flux value

4.4 2008-2016 vs 2021 comparison

In order to compare the two data sets, the spectra were overlaid, as seen in figure 33. The 2021 data resulted in a marginally softer spectrum when compared to the 2008-2016 quiescent data (but both agree within errors). The maximum energy for the 2008-2016 spectrum was 2.498 TeV, while the maximum energy for the 2021 spectrum was higher at 6.269 TeV. The 2008-2016 dataset produced an integral flux of $(2.6 \pm 0.2) \times 10^{-8}$, and the 2021 dataset produced a higher flux of -2.7 ± 0.09 photons m^{-2} $s^{-}1$. Neither data set showed variability.

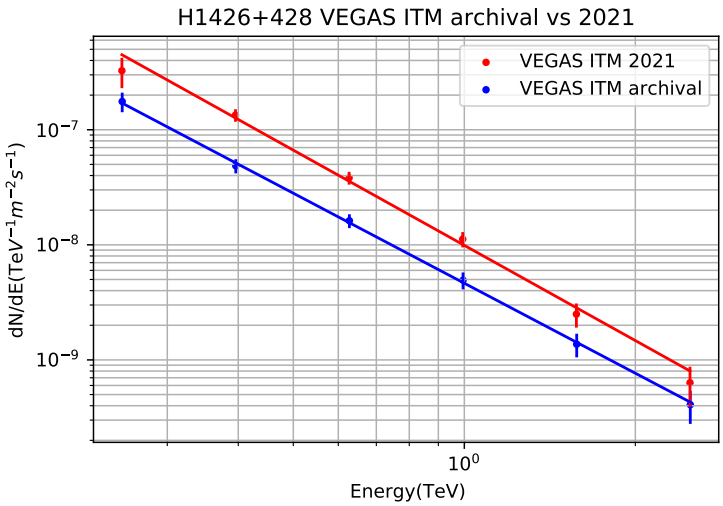

Figure 33: H 1426+428 archival (2008-2016) vs 2021 counts spectra

The EBL corrected spectra for the 2008-2016 and 2021 analyses are compared below in figure 34.

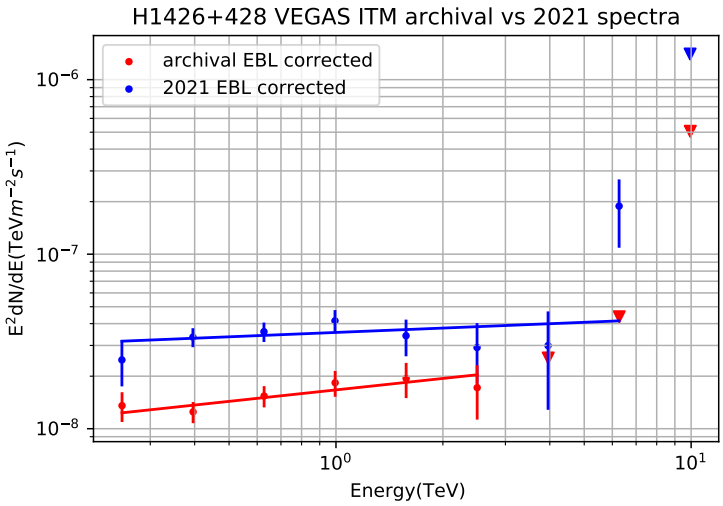

Figure 34: H 1426+428 EBL corrected archival (2008-2016) vs 2021 spectra

Chapter 5: H 1426+428 multi-wavelength data and SED modelling

In this chapter the SSC models for the 2008-2016 and 2021 H 1426+428 MWL SEDs are presented and compared. There are two upcoming VERITAS H 1426+428 papers in progress, one archival with MWL data, and one for 2021. The MWL data has been analysed by collaborators on those papers and the spectral points are included here.

5.1 Instruments and observations

5.1.1 X-ray data

Swift XRT:

The Neil Gehrels Swift observatory [Gehrels et al., 2004] is a satellite with three instruments on board: XRT, BAT and UVOT. Swift XRT (see figure 35) is an X-ray CCD imaging spectrometer designed to measure the fluxes, spectrum and position of gamma-ray bursts (GRBs) and afterglows over a wide dynamic range covering more than 7 orders of magnitude in flux. It has a 110 cm^2 effective area, 23.6×23.6 arcmin FOV, 18 arcsec resolution (half-power diameter), and 0.2-10 keV energy range.

The XRT can pinpoint GRBs to 5-arcsec accuracy within 10 seconds of target acquisition for a typical GRB and can study the X-ray counterparts of GRBs beginning 20-70 seconds from burst discovery and continuing for days to weeks [Burrows et al., 2000]. When the XRT is not following up on GRBs it looks at other targets such as blazars.

The H 1426+428 Swift XRT data were analysed by Ste O'Brien (McGill University) using the publicly available analysis tools. The data contained are taken in both window timing ("WT") and photon counting ("PC") modes. These data were analysed separately using the same spectral binning and corrected for absorption.

For the purpose of constructing the spectral energy distribution all runs taken within one day of a VERITAS run were identified and their spectral fluxes averaged. The Swift XRT data was significantly variable on timescales of days and so a time-scale of 1 day was used for the minimum variability timescale to set a limit on the source size when constructing an SSC model to compare to the SED. The Swift XRT weighted average spectral points are presented in table 12.

Swift BAT:

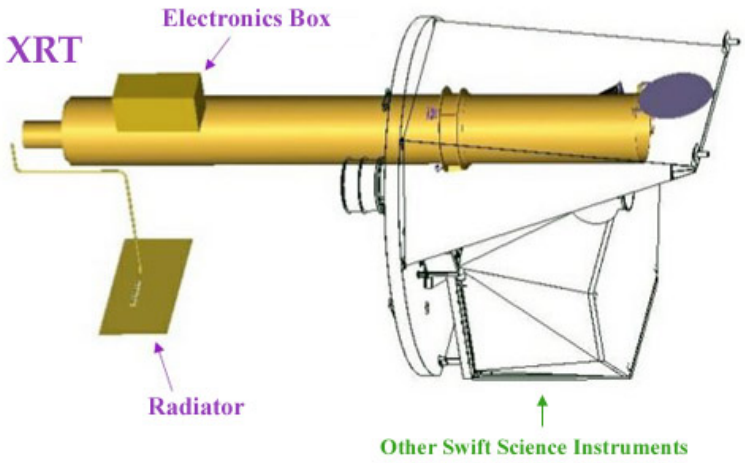

Figure 35: Swift XRT [Hill et al., 2004]

The Burst Alert Telescope (BAT) is designed to provide critical GRB triggers and 4-arcmin positions. It is a highly sensitive, large FOV instrument with a 1.4 steradian field-of-view and an energy range of 15-150 keV for imaging with a non-coded response up to 500 keV. Within several seconds of detecting a burst, the BAT calculates an initial position, decides whether the burst merits a spacecraft slew and, if so, sends the position to the spacecraft.

The BAT (see figure 36) has a large dynamic range and trigger capabilities to enable it to study bursts with a variety of intensities, durations, and temporal structures. It uses a large area solid state detector array and a 2D coded aperture mask to detect weak bursts, and can detect bright bursts due to its large FOV. Long duration gamma-ray emission from the burst can be studied simultaneously with the X-ray and UV/optical emission, as the BAT coded aperture FOV includes both the XRT and UVOT (see below) fields-of-view [Barthelmy et al., 2005].

The Swift BAT data is from the Swift BAT 157 Month Hard X-ray Survey catalogue [Catalogue] which covers the period covers the period MJD 53370 (12-31-2004) to MJD 58115 (12-28-2017). The counts spectrum from the catalogue were converted to flux points using instrument response files provided by the Amy Lien of the Swift BAT catalogue team. Spectral points are shown in table 13.

Table 12: Swift XRT spectral points (E^2dNdE)

E(keV)	F(erg cm^{-2} s^{-1})	Ferr(erg cm^{-2} s^{-1})
0.34	1.26×10^{11}	3.5×10^{13}
0.43	1.42×10^{11}	3.5×10^{13}
0.54	1.54×10^{11}	3.8×10^{13}
0.68	1.67×10^{11}	3.8×10^{13}
0.87	1.71×10^{11}	3.4×10^{13}
1.10	1.72×10^{11}	3.3×10^{13}
1.38	1.83×10^{11}	3.5×10^{13}
1.75	1.88×10^{11}	4.2×10^{13}
2.21	2.05×10^{11}	5.5×10^{13}
2.78	1.95×10^{11}	6.2×10^{13}
3.52	1.90×10^{11}	6.5×10^{13}
4.45	1.99×10^{11}	7.6×10^{13}
5.62	2.09×10^{11}	1.0×10^{13}
7.10	2.14×10^{11}	1.7×10^{13}

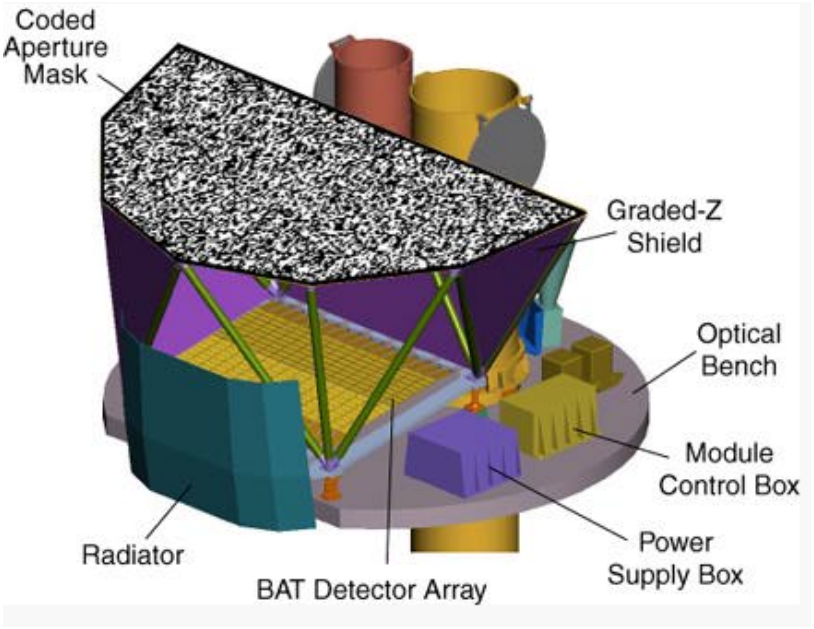

Figure 36: Swift BAT [Barthelmy et al., 2005]

Table 13: Swift BAT spectral points (E^2dNdE)

Energy (keV)	Flux (keV cm^{-2} s^{-1})	Flux error (keV cm^{-2} s^{-1})
16.7	7.3×10^{-3}	3.9×10^{-4}
21.9	6.3×10^{-3}	2.9×10^{-4}
28.9	5.5×10^{-3}	1.9×10^{-4}
41.8	4.6×10^{-3}	3.4×10^{-4}
61.2	3.8×10^{-3}	3.5×10^{-4}
86.6	3.1×10^{-3}	5.8×10^{-4}
122.4	2.6×10^{-3}	5.4×10^{-4}
171.0	2.2×10^{-3}	6.2×10^{-4}

NuSTAR:

NuSTAR (see figure 37) (Nuclear Spectroscopic Telescope Array, also named Explorer 93 and SMEX-11) is a NASA space-based X-ray telescope in its tenth year of operation [Harrison et al., 2013]. It was the first focusing high-energy X-ray telescope in orbit, deployed into a 600 km, near-circular, 6 degree inclination orbit. It focuses high energy X-rays from astrophysical sources using a conical approximation to a Wolter telescope, consisting of two co-aligned grazing-incidence X-ray telescopes pointed at targets by a three-axis stabilized spacecraft. It operates in the range of 3 to 79 keV and concentrates in particular on nuclear spectroscopy. NuSTAR uses a unique deployable mast, or boom, that extended the optics after the payload was in orbit. This allows it to attain the 10m focal length needed [Harrison et al., 2013].

NuSTAR is able to probe the hard X-ray sky with a more than 100-fold improvement in sensitivity over the collimated or coded mask instruments that have operated in this bandpass, due to the inherently low background associated with concentrating the X-ray light.

The 2021 NuSTAR data were analysed by Amy Furniss and Luana de Almeida Pacheco of California State University, East Bay. Spectral points are shown in table 14.

5.1.2 Optical data

Swift UVOT:

Table 14: NuSTAR 2021 spectral points (E^2dNdE)

Energy (keV)	Flux(keV cm^{-2} s^{-1})	Flux error (keV cm^{-2} s^{-1})
3.4	1.36×10^{-2}	3.02×10^{-4}
4.2	1.35×10^{-2}	2.98×10^{-4}
4.9	1.34×10^{-2}	2.98×10^{-4}
5.9	1.38×10^{-2}	3.03×10^{-4}
6.9	1.37×10^{-2}	3.05×10^{-4}
8.2	1.42×10^{-2}	3.17×10^{-4}
9.9	1.40×10^{-2}	3.37×10^{-4}
11.9	1.36×10^{-2}	3.84×10^{-4}
15.5	1.40×10^{-2}	4.16×10^{-4}
24.4	1.45×10^{-2}	4.96×10^{-4}
48.9	1.32×10^{-2}	1.03×10^{-3}

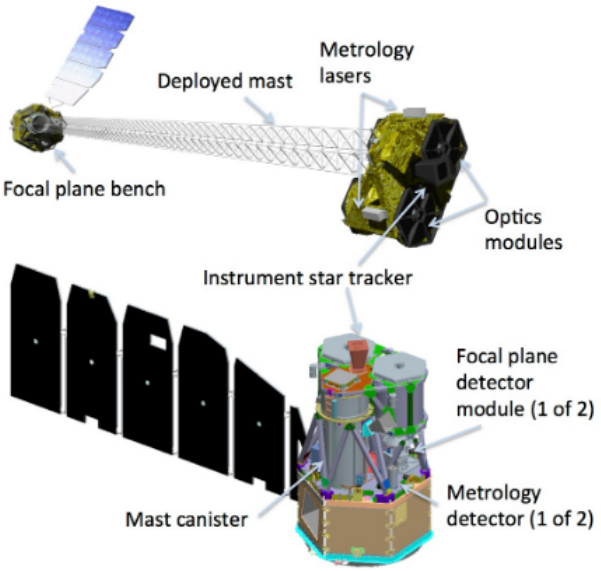

Figure 37: NuSTAR [Caltech, 2022]

The UltraViolet and Optical Telescope (UVOT) (see figure 38) is a diffraction-limited 30 cm (12" aperture) Ritchey-Chrétien reflector, sensitive to magnitude 22.3 in a 17 minute exposure. It is co-aligned with the X-ray Telescope and mounted on the telescope platform common to all instruments. It has an energy range of 170-650

nm. The UVOT aperture is small, but it is still a very useful complement to other instruments because of its UV capabilities and the absence of atmospheric extinction, diffraction, and background [Myers, 2022].

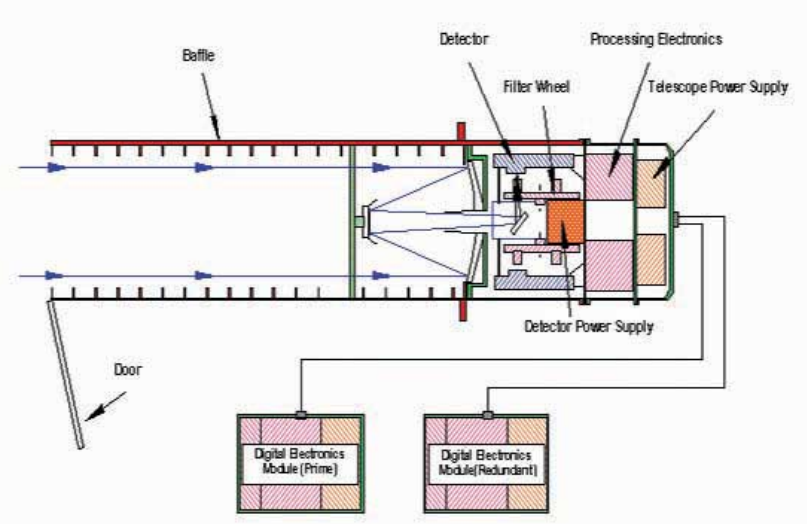

Figure 38: Swift UVOT (the arrows denote the path of light through the telescope) [Myers, 2022]

The UVOT data for six broadband filters were analysed by Deirdre Horan (Ecole Polytechnique) using the publicly available analysis tools. Counts for the source region were determined using a 5.0 arcsec region around the source and the background was estimated using regions of the same size near the source. The magnitudes were determined and then converted to fluxes after correcting for extinction. As for the optical, data taken within one day of VERITAS observations were averaged to determine the weighted mean flux and error for the spectral energy distribution plot. See table 15 for data points.

Table 15: Swift UVOT data points

Filter	runs within 1 day	central freq of filter (log10ν)	flux(erg cm^{-2} s^{-1})	flux error(erg cm^{-2} s^{-1})
1	20	14.841	3.67×10^{-12}	5.15×10^{-14}
2	19	15.129	3.24×10^{-12}	4.83×10^{-14}
3	20	14.933	3.11×10^{-12}	4.30×10^{-14}
4	19	14.745	5.32×10^{-12}	8.89×10^{-14}
5	23	15.057	2.79×10^{-12}	3.84×10^{-14}
6	20	15.170	3.29×10^{-12}	3.82×10^{-14}

FLWO:

The Fred Lawrence Whipple Observatory (FLWO) 1.2-Meter Telescope is a general purpose optical telescope designed to produce images of a wide variety of astronomical objects [CfA, 2022].

The optical data were collected with the 48" optical telescope at the Fred Lawerence Whipple Observatory as part of the Blazar Monitoring Program, which aims to monitor more than 100 blazars to analyse their variability. The data were collected using four filters (R, I, V, B) as shown in table 16 below. The data were analysed by Piata Lusen at the University of California, Santa Cruz.

For each image of H 1426+428 recorded an image of a reference star was also taken and these were used to remove outliers due to weather and unfavourable atmospheric conditions. The magnitudes in each filter were then converted into fluxes. For the purpose of constructing the spectral energy distribution, all runs taken within one day of a VERITAS observation were identified and the weighted average and its uncertainly were determined. No optical data were available at the time of writing for the 2021 data set.

5.1.3 Gamma-ray data

Fermi LAT:

The Fermi Large Area Telescope (Fermi-LAT) (see figure 39) is a gamma-ray experiment installed on the Fermi Gamma-ray Space Telescope [Atwood et al., 2009]. It has been detecting photons in the energy range between 30MeV and 300GeV since 2008. It has a very large field of view, which makes it ideal for the study of flaring

Table 16: FLWO data

Filter	λ_c (μm)	No. of runs within 1 day of VERITAS	Weighted Flux (erg/s/cm^2)
r	0.623	33	$(4.60 \pm 0.03) \times 10^{-12}$
i	0.764	33	$(5.06 \pm 0.03) \times 10^{-12}$
V	0.550	35	$(4.00 \pm 0.05) \times 10^{-12}$
B	0.440	39	$(3.23 \pm 0.02) \times 10^{-12}$

and burst-like sources (such as flares of super-massive black holes, gamma-ray bursts, and solar flares), as it can almost continuously monitor the whole sky.

The LAT is a pair conversion detector, and determines the incident photon directions via the reconstruction of the trajectories of the resulting e+e- pairs. It rejects background events using an anti-coincidence detector (ACD), consisting of scintillator tiles. The baseline LAT is modular, consisting of a 4 x 4 array of identical towers. Each 40 $\times$ 40 cm^2 tower comprises a tracker, calorimeter and data acquisition module [Meyers, 2016].

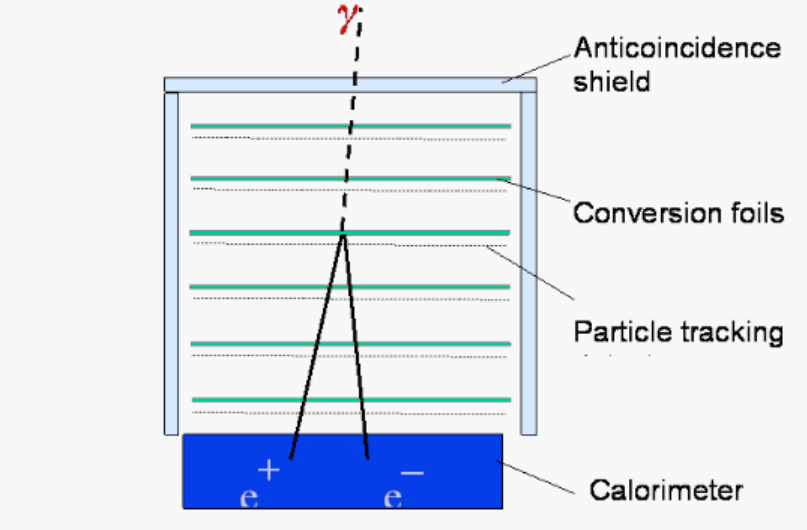

Figure 39: Schematic structure of the LAT [Meyers, 2016]

The Fermi LAT data from MJD 54683 to 57607 (2008-08-05 - 2016-08-07) were analysed with the Fermitools v1.2.23 using the P8R3_SOURCE_V2 instrument re-

sponse functions by Deirdre Horan (Ecole Polytechnique). The sky region around H 1426+428 was iteratively modelled including nearby sources as well as diffuse galactic and extragalactic emission to ensure that the emission from H 1426+428 was accurately determined. The overall differential photon spectrum was well fit by a power-law model. This model was then used to derive the spectral flux points in a series of logarithmically spaced energy bins between 100 MeV and 500 GeV. The spectral points are shown in table 17.

The Fermi LAT data from MJD 59232 to 59350 (2021-01-18 - 2021-05-16) were analysed with the ScienceTools (v2.0.8) via the Fermipy (v1.0.1) python package and using the P8R2 SOURCE V2 instrument response functions by Stephan O'Brien (McGill). A joint-likelihood fit was performed with different event classes (4, 8, 16, 32) handled separately. A sky region of radius 15 degrees centred on H 1426+428 was modelled including nearby sources identified in the 4FGL catalogue, as well as diffuse galactic (gll_iem_v07) and extragalactic emission (iso_P8R2_SOURCE_V6_v06) to ensure that the emission from H 1426+428 was accurately determined. Sources within 5 degrees of H 1426+428 and any source with a test statistic > 10 were fit with their spectral shape parameters fixed to the 4FGL values and their spectral normalization allowed to vary. Sources with test statistic > 50 were fit with their spectral parameters unconstrained. The overall differential photon spectrum was well fit by a power-law model. This model was then used to derive the spectral flux points in a series of logarithmically spaced energy bins between 100 MeV and 300 GeV. The spectral points are shown in table 18.

Table 17: Fermi LAT 2008 - 2016 spectral points (E^2dNdE)

Energy (GeV)	Flux (GeV cm^{-2} s-1)	Flux error (GeV cm^{-2} s^{-1})
2.7×10^{-1}	2.5×10^{-10}	1.9×10^{-10}
4.9×10^{-1}	2.3×10^{-10}	1.1×10^{-10}
8.8×10^{-1}	4.5×10^{-10}	9.4×10^{-11}
1.6×10^{0}	3.5×10^{-10}	8.4×10^{-11}
2.9×10^{0}	6.2×10^{-10}	1.2×10^{-10}
5.3×10^{0}	5.7×10^{-10}	1.4×10^{-10}
9.5×10^{0}	7.6×10^{-10}	2.1×10^{-10}
$1.7\times10^{+1}$	1.6×10^{-10}	3.9×10^{-10}
$3.1\times10^{+1}$	9.2×10^{-10}	4.0×10^{-10}
$5.7\times10^{+1}$	3.2×10^{-10}	9.4×10^{-10}
$1.0\times10^{+2}$	3.0×10^{-10}	1.2×10^{-9}
$1.9\times10^{+2}$	1.8×10^{-10}	1.3×10^{-9}

Table 18: Fermi LAT 2021 spectral points (E^2dNdE)

Energy (GeV)	Flux (GeV cm^{-2} s-1)	Flux error (GeV cm^{-2} s^{-1})
2.2×10^{-1}	2.8×10^{-10}	4.9×10^{-10}
1.1×10^{0}	9.9×10^{-11}	3.2×10^{-10}
5.5×10^{0}	5.6×10^{-10}	3.9×10^{-10}
$2.7\times10^{+1}$	2.1×10^{-9}	1.4×10^{-9}
$1.3\times10^{+2}$	1.6×10^{-15}	2.4×10^{-9}

VERITAS:

The VERITAS spectral points for 2008-2016 and 2021 are given in chapter 4.

5.2 Modelling the multi wavelength SEDs

In this chapter the 2008-2016 and the 2021 SEDs for H1426+428 will be modelled. There are two upcoming VERITAS H 1426+428 papers, one on the 2008-2016 archival data set and one on the 2021 data set. The MWL data has been analysed by collaborators on these upcoming papers, and the resultant spectra for both are shown below in figure 40 and figure 41.

The 2008-2016 SED includes data from Swift XRT, Swift BAT, Swift UVOT, FLWO, Fermi LAT, and VERITAS (see figure 40). The 2021 SED includes data from Swift XRT, NuSTAR, Fermi LAT and VERITAS (see figure 41 - it should be noted that the three Fermi-LAT 2021 data points with very large error bars are effectively upper limits). The VERITAS data for both data sets plotted were analysed by me using VEGAS (see chapter 4). The rest of the multi wavelength data are taken from an upcoming publication by VERITAS on H 1426+428.

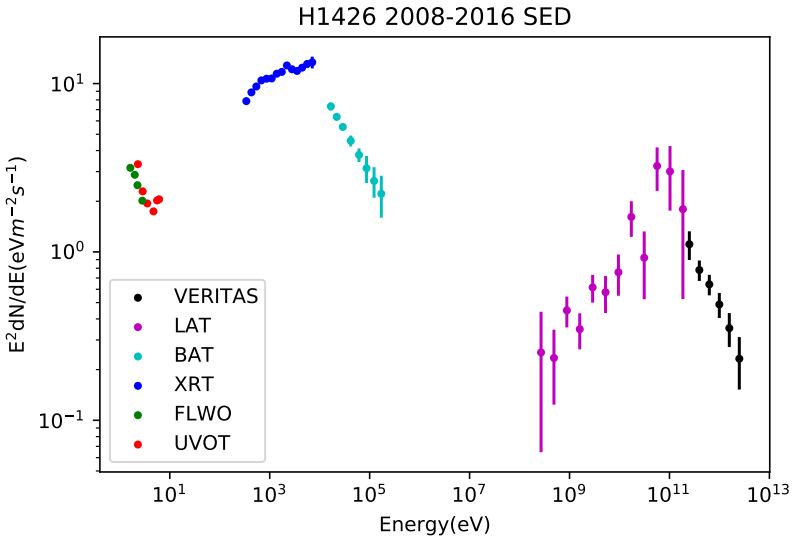

Figure 40: H 1426+428 2008-2016 multiwavelength SED.

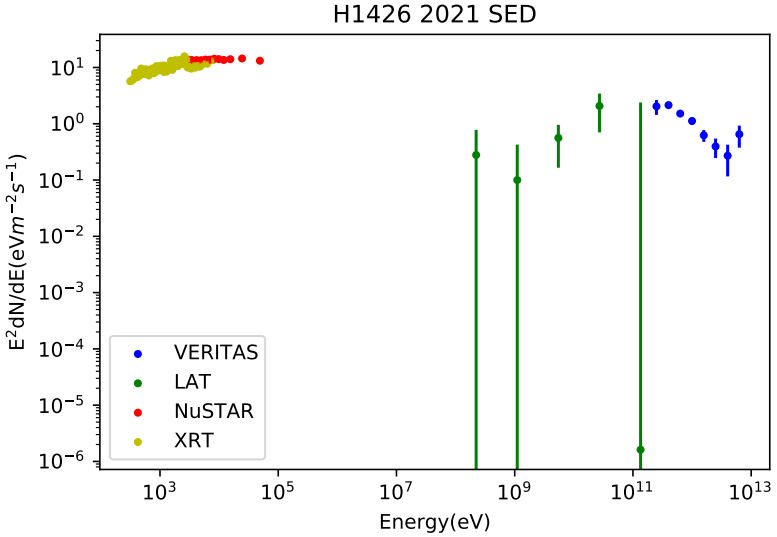

Figure 41: H 1426+428 2021 multiwavelength SED. The first two and the fifth Fermi-LAT data points are effectively upper limits.

The 2008-2016 Swift BAT X-ray data was considerably harder than the NuSTAR 2021 data. The Fermi LAT detection is too weak to really constrain the spectrum

on a timescale of a few months. In 2021 the TeV flux from the source as measured by VERITAS was noticeably higher than before. The spectral slope in the 1-10 keV range as measured by Swift XRT was harder than in previous observations.

The SEDs were modelled using the SSC model of the AGNpy package. The model entails a blob of radius R, whose size is determined from the minimum variability timescale (taken to be one day in this case) with a broken power-law distribution of electron Lorentz factors in a region of magnetic field B. The blob has a bulk Lorentz factor γ_b and a Doppler factor δ. γ_{max} represents the highest energy of the gamma-ray photon observed, and γ_{min} the minimum energy. The complete list of parameters is shown in table 19. The parameters were adjusted manually until a good match, by eye, was seen between the model and the data. Once the 2008-2016 SED had been modelled I then approached modelling the 2021 SED by starting with the 2008-2016 model parameters and changing the minimum number until agreement was found. Gammapy was used to produce the SED after EBL absorption.

Table 19: Parameters for the SSC model

Params	2008-2016	2021
Spectrum norm	5.5×10^{47} ergs	5.5×10^{47} ergs
z	0.129	0.129
B	5.7×10^{-3} G	5.7×10^{-3} G
Doppler factor	37	29
t_{var}	1 day	1 day
p1	2.3	2.1
p2	4.2	2.95
γ_{min}	2×10^3	4.5×10^3
γ_b	1×10^6	1×10^6
γ_{max}	3×10^7	3×10^7
R_b	8.49×10^{16} cm	6.65×10^{16} cm

Figure 42 shows the 2008-2016 SED and model. As can be seen in figure 43 the model required to match the XRT data for 2021 results in quite a different shape for the lower energy hump of the SED in particular. The dotted line in each figure shows the inverse-Compton hump of the SED before EBL absorption. In figure 44 the model for the 2021 data and the model for the 2008-2016 data are plotted on the same graph in order to compare.

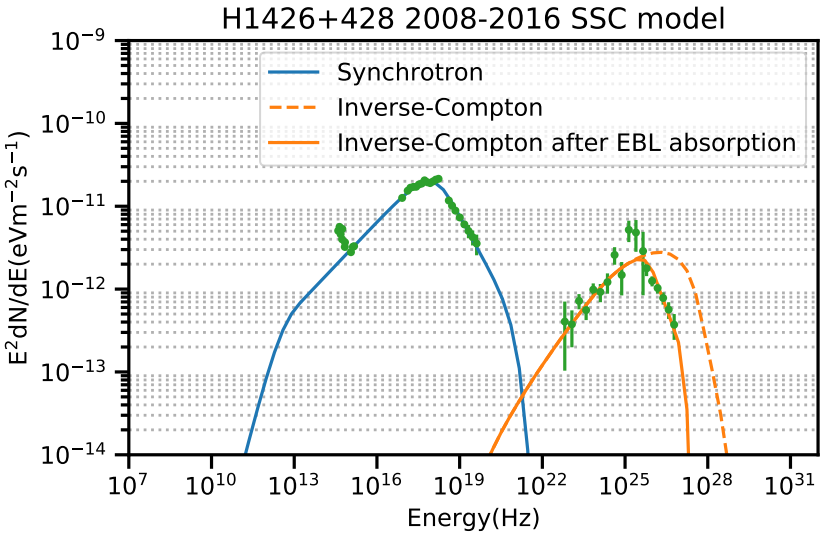

Figure 42: H 1426+428 2008-2016 SED SSC model with parameters given in table 19

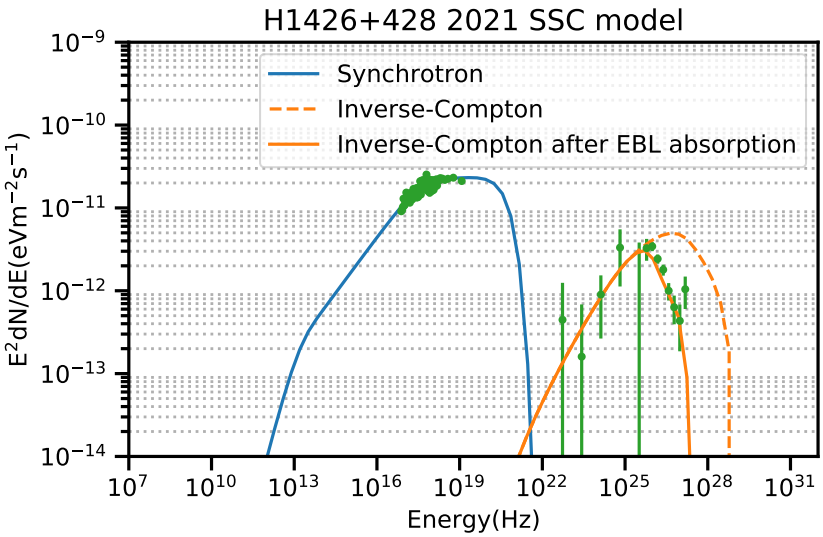

Figure 43: H 1426+428 2021 SED SSC model with parameters given in table 19

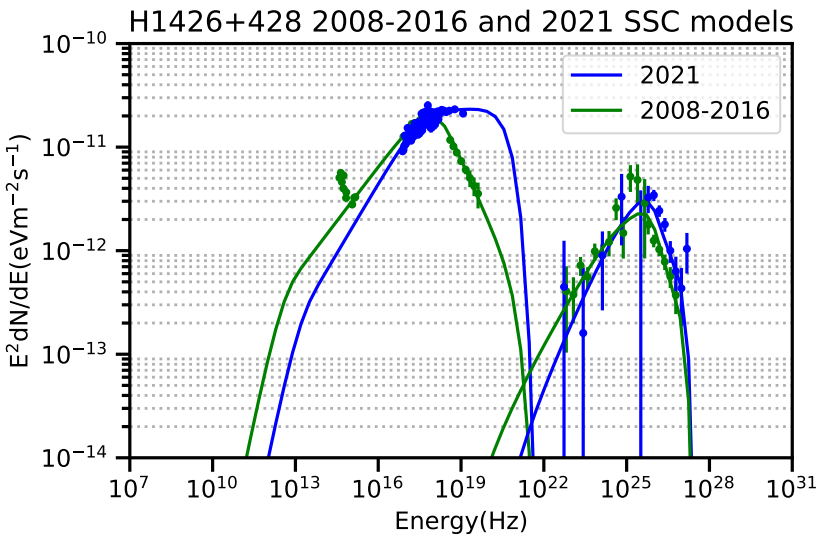

Figure 44: H 1426+428 2008-2016 and 2021 SED models plotted together

The parameters γ_{min} and γ_{max} are difficult to estimate, as γ_{max} represents the highest energy of the gamma-ray photon observed, and the high energy tail of the blazar SED is affected by Klein-Nishina effects (while the low energy end of is affected by synchrotron self absorption). γ_{min} is a weak parameter, however, and doesn't have a huge bearing on the overall fit. The spherical emission region parameters (for the most part) remained the same for SEDs, as the source in both cases is the same. These include B (the magnetic field tangled to the jet), z (redshift), t_{var} (timescale), R_b (the radius of the blob) and the Doppler factor. The Doppler factor needed to be changed to accurately fit the 2021 data, and as the blob radius is calculated based on the Doppler factor and the redshift ($R_b = (ct_{var}D)/(1+z)$), the blob radius ended up being slightly different in both models ($R_b = 8.49 \times 10^{16}$ for 2008-2016, and $R_b = 6.65 \times 10^{16}$ for 2021).

Of the electron spectrum parameters for the broken power law fit, γ_{max} was unchanged ($\gamma_{max} = 3 \times 10^7$) between the two data sets. Parameters p1 and p2 were changed slightly (2.3 and 4.2 respectively for the 2008-2016 data, and 2.1 and 2.95 respectively for the 2021 data), γ_{min} was higher in the 2021 fit ($\gamma_{min} = 4.5 \times 10^3$) compared to the 2008-2016 fit ($\gamma_{min} = 2 \times 10^3$), and γ_b was slightly different also ($\gamma_b = 1 \times 10^6$) in the 2021 fit and in $\gamma_{min} = 1.2 \times 10^6$) the 2008-2016 fit). The SSC model does not match the optical points in either case but it was chosen to overlook this.

Chapter 6: Conclusions

This thesis has looked at the HBL blazar H 1426+428 during two time periods, an 8 year quiescent data set from 2008 to 2016, and a period of higher activity in 2021. Both datasets were analysed separately using VERITAS analysis software VEGAS to test for a clear detection of the source and to derive a time-averaged spectrum.

The 2008-2016 data set showed a strong detection with a significance of 18.8σ. The 2021 data set also showed a clear detection with a significance of 20.5σ. The sky maps for both datasets indicated clear excesses at the location of H 1426+428 with no additional sources present. The significance distributions also indicated a clear excess due to the source in both cases which was not visible when the source was excluded. The significance distributions both looked statistically significant and gave confidence in the analysis and source location of maximum significance.

The 2008-2016 dataset had an integral flux above 0.25 TeV of $(2.6 \pm 0.2) \times 10^{-8}$ photons m^{-2} s^{-1}, which corresponds to a flux of $\sim$ 1.5% Crab. The 2021 data set had a significantly higher flux above 0.25 TeV, at $(2.7 \pm 0.2) \times 10^{-8}$ photons m^{-2} s^{-1}, which corresponds to a flux of $\sim$ 1.6% Crab.

Both spectra were found to fit satisfactorily with a power law model. The EBL attenuation factors for both spectra were calculated using the model of Francescini et al (2008) (included in the Gammapy package), and were used to de-absorb the spectral points. The absorbed and de-absorbed spectral energy density points were then compared. Different timescales (daily, monthly, and yearly) were investigated for flux variability by calculating the χ^2 values and probabilities for constant flux. It was concluded that the VERITAS data showed no significant flaring episodes, though there is some evidence of year-to-year variability in the data.

These analyses were used as secondary analyses for two upcoming VERITAS papers on the archival (2008-2016) data set and on the 2021 data set, and the primary analyses agreed very well in both cases.

The two H 1426+428 SEDs were modelled using the SSC model of the AGNpy package, with Gammapy used to show the SED after EBL absorption. It was found that the two states could be modelled by keeping the magnetic field parameter the same, but a different Doppler factor and changes to some of the electron energy distribution parameters were required. The 2021 data required a higher gamma min parameter and a lower gamma b. Parameters p1 and p2 were also changed slightly between the two analyses. The SSC model did not match the optical data in either case.

To take this aspect of the project further, the next steps would be to fit a model to find the optimum parameters rather changing them manually. This would require adding systematic errors for each instrument, or scanning ranges of parameters to derive confidence intervals.

Further avenues of interest involving this project could be to compare H 1426+428 to other extreme HBL blazars and see if similar parameters would be required to model the SEDs. It would also be interesting to repeat the analysis when future generations of Cherenkov telescopes with greater sensitivity (such as the Cherenkov Telescope Array) observe H 1426+428.

Appendix

A description of some of the code written for this research:

VEGAS IRF selection and automatic analysis script: I contributed to a python script which requires the input of a runlist in order to search the database and produce the appropriate IRFs required for either a standard or ITM analysis of the runs. It can then (if the option is selected) run an automatic standard or ITM analysis on the runlist (as opposed to having to analyse each run separately) for VEGAS stages 1 - 5. Options can be inputted for stage 4 and 5 cuts (soft, medium or hard cuts), type of data, time cuts, VEGAS stages to run etc.

Lightcurve script: I wrote a bash script which involves the input of a runlist, with options to divide on a nightly, weekly, or yearly basis, and options for analysis specifications. The code then creates separate runlists for each night/month/year and runs a stage 6 VEGAS analysis with appropriate EAs on each one, producing fluxes which are then plotted against MJD to produce lightcurves.

EBL script: I wrote a python script which uses the gammapy package to evaluate the optical depth function for each energy bin of a spectrum. It then divides the flux by the optical depth function to show the EBL corrected spectrum, and plots the corrected spectrum against the original for comparison.

References

AA Abdo, Markus Ackermann, Marco Ajello, William B Atwood, Magnus Axelsson, Luca Baldini, Jean Ballet, Guido Barbiellini, Matthew G Baring, D Bastieri, et al. Fermi observations of tev-selected active galactic nuclei. *The Astrophysical Journal*, 707(2):1310, 2009.

Bannanje Sripathi Acharya, Iván Agudo, Imen Al Samarai, R Alfaro, J Alfaro, C Alispach, R Alves Batista, JP Amans, E Amato, G Ambrosi, et al. Science with the cherenkov telescope array. 2017.

Markus Ackermann, M Ajello, WB Atwood, Luca Baldini, J Ballet, G Barbiellini, D Bastieri, J Becerra Gonzalez, R Bellazzini, E Bissaldi, et al. The third catalog of active galactic nuclei detected by the fermi large area telescope. *The Astrophysical Journal*, 810(1):14, 2015.

F Aharonian, A Akhperjanian, J Barrio, M Beilicke, K Bernlöhr, H Börst, H Bojahr, O Bolz, J Contreras, R Cornils, et al. Tev gamma rays from the blazar h 1426+ 428 and the diffuse extragalactic background radiation. *Astronomy & Astrophysics*, 384(3):L23–L26, 2002.

F Aharonian, A Akhperjanian, M Beilicke, K Bernlöhr, H-G Börst, H Bojahr, O Bolz, T Coarasa, JL Contreras, J Cortina, et al. Observations of 54 active galactic nuclei with the hegra system of cherenkov telescopes. *Astronomy & Astrophysics*, 421(2): 529–537, 2004.

FA Aharonian and G Heinzelmann. The hegra experiment-status and recent results. *arXiv preprint astro-ph/9702059*, 1997.

Jelena Aleksić, S Ansoldi, Lucio Angelo Antonelli, P Antoranz, A Babic, P Bangale, M Barceló, JA Barrio, J Becerra González, W Bednarek, et al. The major upgrade of the magic telescopes, part ii: A performance study using observations of the crab nebula. *Astroparticle Physics*, 72:76–94, 2016.

S Archambault, A Archer, W Benbow, R Bird, E Bourbeau, A Bouvier, M Buchovecky, V Bugaev, JV Cardenzana, M Cerruti, et al. Gamma-ray observations under bright moonlight with veritas. *Astroparticle Physics*, 91:34–43, 2017a.

S Archambault, A Archer, W Benbow, R Bird, E Bourbeau, T Brantseg, M Buchovecky, JH Buckley, V Bugaev, K Byrum, et al. Dark matter constraints from a joint analysis of dwarf spheroidal galaxy observations with veritas. *arXiv preprint arXiv:1703.04937*, 2017b.

WB Atwood, Aous A Abdo, Markus Ackermann, W Althouse, B Anderson, M Axelsson, Luca Baldini, J Ballet, DL Band, Guido Barbiellini, et al. The large area telescope on the fermi gamma-ray space telescope mission. *The Astrophysical Journal*, 697(2):1071, 2009.

Saugata Barat, Ritaban Chatterjee, and Kaustav Mitra. Locating the gev emission region in the jets of blazars from months time-scale multiwavelength outbursts. *Monthly Notices of the Royal Astronomical Society*, 515(2):1655–1662, 2022.

Scott D Barthelmy, Louis M Barbier, Jay R Cummings, Ed E Fenimore, Neil Gehrels, Derek Hullinger, Hans A Krimm, Craig B Markwardt, David M Palmer, Ann Parsons, et al. The burst alert telescope (bat) on the swift midex mission. *Space Science Reviews*, 120(3):143–164, 2005.

Wystan Benbow. Highlights of the veritas blazar observation program. *arXiv preprint arXiv:1110.0038*, 2011.

M Böttcher, A Reimer, K Sweeney, and A Prakash. Leptonic and hadronic modeling of fermi-detected blazars. *The Astrophysical Journal*, 768(1):54, 2013.

David N Burrows, Joanne E Hill, John A Nousek, Alan A Wells, Alexander T Short, Richard Willingale, Oberto Citterio, Guido Chincarini, and G Tagliaferri. Swift x-ray telescope. In *X-Ray and Gamma-Ray Instrumentation for Astronomy XI*, volume 4140, pages 64–75. SPIE, 2000.

Caltech, Feb 2022. URL `https://www.nustar.caltech.edu/`.

Bradley W Carroll and Dale A Ostlie. *An introduction to modern astrophysics*. Cambridge University Press, 2017.

J-M Casandjian and Isabelle A Grenier. A revised catalogue of egret-ray sources. *Astronomy & Astrophysics*, 489(2):849–883, 2008.

Swift Catalogue. Swift catalogue. `https://swift.gsfc.nasa.gov/results/bs157mon/`.

Harvard-Smithsonian CfA. FLWO. `http://www.sao.arizona.edu/FLWO/48/48.html`, 2022. Accessed: 2022-28-08.

Xuhui Chen, Martin Pohl, and Markus Böttcher. Particle diffusion and localized acceleration in inhomogeneous agn jets–i. steady-state spectra. *Monthly Notices of the Royal Astronomical Society*, 447(1):530–544, 2015.

Jodi Christiansen. Characterization of a maximum likelihood gamma-ray reconstruction algorithm for veritas. *arXiv preprint arXiv:1708.05684*, 2017.

P Cogan. Vegas, the veritas gamma-ray analysis suite. *arXiv preprint arXiv:0709.4233*, 2007.

L Costamante, G Ghisellini, P Giommi, G Tagliaferri, A Celotti, M Chiaberge, G Fossati, L Maraschi, F Tavecchio, A Treves, et al. Extreme synchrotron bl lac objects-stretching the blazar sequence. *Astronomy & Astrophysics*, 371(2):512–526, 2001.

John M Davies and Eugene S Cotton. Design of the quartermaster solar furnace. *Solar Energy*, 1(2-3):16–22, 1957.

Arache Djannati-Atai, B Khelifi, S Vorobiov, R Bazer-Bachi, LM Chounet, G Debiais, B Degrange, P Espigat, B Fabre, G Fontaine, et al. Detection of the bl lac object 1es 1426+ 428 in the very high energy gamma-ray band by the cat telescope from 1998–2000. *Astronomy & Astrophysics*, 391(3):L25–L28, 2002.

Herve Dole, Guilaine Lagache, J-L Puget, Karina I Caputi, Nestor Fernandez-Conde, E Le Floc'h, Casey Papovich, Pablo G Pérez-González, George H Rieke, and Myra Blaylock. The cosmic infrared background resolved by spitzer-contributions of mid-infrared galaxies to the far-infrared background. *Astronomy & Astrophysics*, 451 (2):417–429, 2006.

Camden Ertley. *Studying the polarization of hard x-ray solar flares with the Gamma RAy Polarimeter Experiment (GRAPE)*. PhD thesis, University of New Hampshire, 2014.

Warren Essey and Alexander Kusenko. A new interpretation of the gamma-ray observations of distant active galactic nuclei. *Astroparticle Physics*, 33(2):81–85, 2010.

Renato Falomo, Elena Pian, and Aldo Treves. An optical view of bl lacertae objects. *The Astronomy and Astrophysics Review*, 22(1):73, 2014.

Xu-Liang Fan and Qingwen Wu. Jet power of jetted active galactic nuclei: Implications for evolution and unification. *The Astrophysical Journal*, 879(2):107, 2019.

Nicole Fields. A multi-wavelength blazar campaign. *BULLETIN-AMERICAN ASTRONOMICAL SOCIETY*, 39(4):004, 2007.

G al Fossati, L Maraschi, A Celotti, A Comastri, and G Ghisellini. A unifying view of the spectral energy distributions of blazars. *Monthly Notices of the Royal Astronomical Society*, 299(2):433–448, 1998.

M Fouka and S Ouichaoui. Analytical fits for the synchrotron emission from a power-law particle distribution with a sharp cutoff. *Monthly Notices of the Royal Astronomical Society*, 442(2):979–994, 2014.

Alberto Franceschini, Giulia Rodighiero, and Mattia Vaccari. Extragalactic optical-infrared background radiation, its time evolution and the cosmic photon-photon opacity. *Astronomy & Astrophysics*, 487(3):837–852, 2008.

Giorgio Galanti, Fabrizio Tavecchio, and Marco Landoni. Fundamental physics with blazar spectra: a critical appraisal. *Monthly Notices of the Royal Astronomical Society*, 491(4):5268–5276, 2020.

W Galbraith and JV Jelley. Light pulses from the night sky associated with cosmic rays. *Nature*, 171(4347):349–350, 1953.

Neil Gehrels, Guido Chincarini, P ea Giommi, KO Mason, JA Nousek, AA Wells, NE White, SD Barthelmy, DN Burrows, LR Cominsky, et al. The swift gamma-ray burst mission. *The Astrophysical Journal*, 611(2):1005, 2004.

Markos Georganopoulos and Demosthenes Kazanas. Decelerating flows in tev blazars: a resolution to the bl lacertae-fr i unification problem. *The Astrophysical Journal*, 594(1):L27, 2003.

G Ghisellini, L Maraschi, and L Dondi. Diagnostics of inverse-compton models for the gamma-ray emission of 3c 279 and mkn 421. *Astronomy and Astrophysics Supplement Series*, 120:503–506, 1996.

Gabriele Ghisellini, Fabrizio Tavecchio, and Marco Chiaberge. Structured jets in tev bl lac objects and radiogalaxies-implications for the observed properties. *Astronomy & Astrophysics*, 432(2):401–410, 2005.

Gabriele Ghisellini, L Maraschi, and F Tavecchio. The fermi blazars' divide. *Monthly Notices of the Royal Astronomical Society: Letters*, 396(1):L105–L109, 2009.

Gabriele Ghisellini, Fabrizio Tavecchio, L Maraschi, A Celotti, and T Sbarrato. The power of relativistic jets is larger than the luminosity of their accretion disks. *Nature*, 515(7527):376–378, 2014.

Riccardo Giacconi, S Murray, H Gursky, E Kellogg, E Schreier, and H Tananbaum. The uhuru catalog of x-ray sources. *The Astrophysical Journal*, 178:281–308, 1972.

Berrie Giebels and HESS Collaboration. Status and recent results from hess. *arXiv preprint arXiv:1303.2850*, 2013.

J Guy, C Renault, FA Aharonian, M Rivoal, and J-P Tavernet. Constraints on the cosmic infra-red background based on bepposax and cat spectra of mkn 501. *Arxiv preprint astro-ph/0004355*, 2000.

J Hall, VV Vassiliev, DB Kieda, J Moses, T Nagai, and J Smith. Veritas cfds. In *International Cosmic Ray Conference*, volume 5, page 2851, 2003.

Fiona A Harrison, William W Craig, Finn E Christensen, Charles J Hailey, William W Zhang, Steven E Boggs, Daniel Stern, W Rick Cook, Karl Forster, Paolo Giommi, et al. The nuclear spectroscopic telescope array (nustar) high-energy x-ray mission. *The Astrophysical Journal*, 770(2):103, 2013.

RC Hartman, DL Bertsch, SD Bloom, AW Chen, P Deines-Jones, JA Esposito, CE Fichtel, DP Friedlander, SD Hunter, LM McDonald, et al. The third egret catalog of high-energy gamma-ray sources. *The Astrophysical Journal Supplement Series*, 123(1):79, 1999.

Dieter Heck, Johannes Knapp, JN Capdevielle, G Schatz, T Thouw, et al. Corsika: A monte carlo code to simulate extensive air showers. *Report fzka*, 6019(11), 1998.

Walter Heitler. *The quantum theory of radiation*. Courier Corporation, 1984.

Joanne E Hill, David N Burrows, John A Nousek, Anthony F Abbey, Richard M Ambrosi, Heinrich W Brauninger, Wolfgang Burkert, Sergio Campana, Chaitanya Cheruvu, Giancarlo Cusumano, et al. Readout modes and automated operation of the swift x-ray telescope. In *X-Ray and Gamma-Ray Instrumentation for Astronomy XIII*, volume 5165, pages 217–231. SPIE, 2004.

A Michael Hillas. Cerenkov light images of eas produced by primary gamma. In *19th Intern. Cosmic Ray Conf-Vol. 3*, number OG-9.5-3, 1985.

AM Hillas. Evolution of ground-based gamma-ray astronomy from the early days to the cherenkov telescope arrays. *Astroparticle Physics*, 43:19–43, 2013.

Jamie Holder. Atmospheric cherenkov gamma-ray telescopes. In *The WSPC Handbook of Astronomical Instrumentation: Volume 5: Gamma-Ray and Multimessenger Astronomical Instrumentation*, pages 117–136. World Scientific, 2021.

Jamie Holder, RW Atkins, HM Badran, G Blaylock, SM Bradbury, JH Buckley, KL Byrum, DA Carter-Lewis, O Celik, YCK Chow, et al. The first veritas telescope. *Astroparticle Physics*, 25(6):391–401, 2006.

D Horan, HM Badran, IH Bond, SM Bradbury, JH Buckley, MJ Carson, DA Carter-Lewis, M Catanese, W Cui, S Dunlea, et al. Detection of the bl lacertae object h1426+ 428 at tev gamma-ray energies. *The Astrophysical Journal*, 571(2):753, 2002.

KI Kellermann and IIK Pauliny-Toth. The spectra of opaque radio sources. *The Astrophysical Journal*, 155:L71, 1969.

J Kildea, RW Atkins, HM Badran, G Blaylock, IH Bond, SM Bradbury, JH Buckley, DA Carter-Lewis, O Celik, YCK Chow, et al. The whipple observatory 10 m gamma-ray telescope, 1997–2006. *Astroparticle Physics*, 28(2):182–195, 2007.

John Kormendy and Luis C Ho. Coevolution (or not) of supermassive black holes and host galaxies. *Annual Review of Astronomy and Astrophysics*, 51:511–653, 2013.

Masaaki Kusunose and Fumio Takahara. Compton scattering in the klein-nishina regime revisited. *The Astrophysical Journal*, 621(1):285, 2005.

Marco Landoni, Renato Falomo, Aldo Treves, and Boris Sbarufatti. Spectroscopy of bl lacertae objects of extraordinary luminosity. *Astronomy & Astrophysics*, 570: A126, 2014.

J Lefaucheur, C Deil, A Donath, L Jouvin, B Khélifi, and J King. Gammapy-an open-source python package for γ-ray astronomy. *Astronomical Data Analysis Software and Systems XXVII*, 522:525, 2020.

T-P Li and Y-Q Ma. Analysis methods for results in gamma-ray astronomy. *The Astrophysical Journal*, 272:317–324, 1983.

AP Lightman and GB Rybicki. Inverse compton reflection-time-dependent theory. *The Astrophysical Journal*, 232:882–890, 1979.

Grzegorz Madejski and Marek Sikora. Gamma-ray observations of active galactic nuclei. *Annu. Rev. Astron. Astrophys*, 54:725–760, 2016.

K Mannheim and PL Biermann. Gamma-ray flaring of 3c 279-a proton-initiated cascade in the jet? *Astronomy and Astrophysics*, 253:L21–L24, 1992.

L Maraschi, G Ghisellini, and A Celotti. A jet model for the gamma-ray emitting blazar 3c 279. *The Astrophysical Journal*, 397:L5–L9, 1992.

Apostolos Mastichiadis and Maria Petropoulou. Hadronic x-ray flares from blazars. *The Astrophysical Journal*, 906(2):131, 2021.

A McCann, D Hanna, and M McCutcheon. An alignment system for imaging atmospheric cherenkov telescopes. *arXiv preprint arXiv:0907.4975*, 2009.

J.D. Meyers, Feb 2016. URL `https://fermi.gsfc.nasa.gov/science/eteu/agn/`.

J.D. Myers, Feb 2022. URL https://swift.gsfc.nasa.gov/about_swift/.

T Nagai, R McKay, G Sleege, D Petry, VERITAS Collaboration, et al. Focal plane instrumentation of veritas. *arXiv preprint arXiv:0709.4517*, 2007.

C Nigro, J Sitarek, P Gliwny, D Sanchez, A Tramacere, and M Craig. agnpy: an open-source python package modelling the radiative processes of jetted active galactic nuclei. *arXiv preprint arXiv:2112.14573*, 2021.

Mohamed Omer and Ryoichi Hajima. Geant4 physics process for elastic scattering of γ-rays. Technical report, Japan Atomic Energy Agency, 2018.

Nahee Park. Performance of the veritas experiment. *arXiv preprint arXiv:1508.07070*, 2015.

Andrii Petrashyk. *Advancements in Very-High-Energy Gamma-Ray Astronomy with Applications to the Study of Cosmic Rays*. Columbia University, 2019.

John Quinn and VERITAS Collaboration. VERITAS detection of an elevated VHE flux from the blazar H 1426+428. *The Astronomer's Telegram*, 14501:1, March 2021.

PF Rebillot, JH Buckley, P Dowkontt, and K Kosack. The veritas flash adc electronics system. In *International Cosmic Ray Conference*, volume 5, page 2827, 2003.

RA Remillard, IR Tuohy, RJV Brissenden, DAH Buckley, DA Schwartz, ED Feigelson, and S Tapia. Two x-ray-selected bl lacertae objects observed with the heao 1 scanning modulation collimator. *The Astrophysical Journal*, 345:140–147, 1989.

E Roache, R Irvin, JS Perkins, K Harris, A Falcone, J Finley, and T Weekes. Mirror facets for the veritas telescopes. In *International Cosmic Ray Conference*, volume 3, pages 1397–1400, 2008.

M Nievas Rosillo. The throughput calibration of the veritas telescopes. *arXiv preprint arXiv:2108.10283*, 2021.

George B Rybicki and Alan P Lightman. *Radiative processes in astrophysics*. John Wiley & Sons, 1991.

Govert Schilling. Quasars or blazars? it's all in the angle. *Science*, 292(5524): 1985–1985, 2001. ISSN 0036-8075. doi: 10.1126/science.292.5524.1985a. URL https://science.sciencemag.org/content/292/5524/1985.1.

Fabrizio Tavecchio and Gabriele Ghisellini. Spine–sheath layer radiative interplay in subparsec-scale jets and the tev emission from m87. *Monthly Notices of the Royal Astronomical Society: Letters*, 385(1):L98–L102, 2008.

Fabrizio Tavecchio, Laura Maraschi, and Gabriele Ghisellini. Constraints on the physical parameters of tev blazars. *The Astrophysical Journal*, 509(2):608, 1998.

DJ Thompson. Gamma ray astrophysics: the egret results. *Reports on Progress in Physics*, 71(11):116901, 2008.

Marie-Helene Ulrich, Laura Maraschi, and C Megan Urry. Variability of active galactic nuclei. *Annual Review of Astronomy and Astrophysics*, 35(1):445–502, 1997.

C Megan Urry and Paolo Padovani. Unified schemes for radio-loud active galactic nuclei. *Publications of the Astronomical Society of the Pacific*, 107(715):803, 1995.

Vinay Venugopal and Piyush S Bhagdikar. de broglie wavelength and frequency of the scattered electrons in compton effect. *arXiv preprint arXiv:1202.4572*, 2012.

VERITAS homepage, Jan 2004. URL `https://veritas.sao.arizona.edu/`.

W Thomas Vestrand. Gamma-ray astronomy. *Encyclopedia of Physical Science and Technology*, 6:397, 2002.

Trevor C Weekes. The atmospheric cherenkov imaging technique for very high energy gamma-ray astronomy. *arXiv preprint astro-ph/0508253*, 2005.

Trevor C Weekes, Michael F Cawley, DJ Fegan, KG Gibbs, AM Hillas, PW Kowk, RC Lamb, DA Lewis, DJ Macomb, NA Porter, et al. Observation of tev gamma-rays from the crab nebula using the atmospheric cherenkov imaging technique. *Astrophysical Journal*, 342:379–395, 1989.

A Weinstein. The veritas trigger system. *arXiv preprint arXiv:0709.4438*, 2007.

Roland Winston. Light collection within the framework of geometrical optics. *Josa*, 60(2):245–247, 1970.

AG Wright. *The photomultiplier handbook*. Oxford University Press, 2017.

Yuji Yazaki. How the klein–nishina formula was derived: Based on the sangokan nishina source materials. *Proceedings of the Japan Academy, Series B*, 93(6):399–421, 2017.